Continental Shelf Research 31 (2011) 539–554

Contents lists available at ScienceDirect

Continental Shelf Research

journal homepage: www.elsevier.com/locate/csr

Research papers

Thermal and haline variability over the central Bering Sea shelf: Seasonal and interannual perspectives

S. Danielson [a,*], L. Eisner [b], T. Weingartner [a], K. Aagaard [c]

[a] School of Fisheries and Ocean Science, Institute of Marine Science, University of Alaska Fairbanks, Rm. 114 O'Neill Building, Fairbanks, AK 99775-7220, USA
[b] National Oceanic and Atmospheric Administration, National Marine Fisheries Service, Alaska Fisheries Science Center, Ted Stevens Marine Research Institute, Juneau, AK, USA
[c] Polar Science Center, Applied Physics Laboratory, University of Washington, Seattle, WA, USA

ARTICLE INFO

Article history:
Received 22 May 2010
Received in revised form
9 December 2010
Accepted 17 December 2010
Available online 23 December 2010

Keywords:
Bering Sea
Seasonal variability
Interannual variability
Temperature
Salinity
Ekman transport

ABSTRACT

We examine multi-year conductivity-temperature-depth (CTD) data to better understand temperature and salinity variability over the central Bering Sea shelf. Particular consideration is given to observations made annually from 2002 to 2007 between August and October, although other seasons and years are also considered. Vertical and horizontal correlation maps show that near-surface and near-bottom salinity anomalies tend to fluctuate in phase across the central shelf, but that temperature anomalies are vertically coherent only in the weakly or unstratified inner-shelf waters. We formulate heat content (HC) and freshwater content (FWC) budgets based on the CTD observations, direct estimates of external fluxes (surface heat fluxes, ice melt, precipitation (P), evaporation (E) and river discharge), and indirect estimates of advective contributions. Ice melt, $P-E$, river discharge, and along-isobath advection are sufficient to account for the mean spring-to-fall increase in FWC, while summer surface heat fluxes are primarily responsible for the mean seasonal increase in HC, although interannual variability in the HC at the end of summer appears related to variability in the along-isobath advection during the summer months. On the other hand, FWC anomalies at the end of summer are significantly correlated with the mean wind direction and cross-isobath Ekman transport averaged over the previous winter. Consistent with the latter finding, salinities exhibit a weak but significant inverse correlation between the coastal and mid-shelf waters. The cross-shelf transport likely has significant effect on nutrient fluxes and other processes important to the functioning of the shelf ecosystem. Both the summer and winter advection fields appear to result from the seasonal mean position and strength of the Aleutian Low. We find that interannual thermal and haline variability over the central Bering Sea shelf are largely uncoupled.

1. Introduction

The enormous biological production of the Bering Sea shelf (Fig. 1) is evident in its primary productivity (Sambrotto et al., 1986; Walsh et al., 1989; Springer et al., 1996), commercial fisheries (Failor-Rounds, 2005; Bowers et al., 2008), and large marine mammal populations (Lowry et al., 1982). While there are apparent connections between variations in climate and biological production (Grebmeier et al., 2006; Zheng and Kruse, 2006; Aydin and Mueter, 2007), the physical mechanisms underlying these linkages are poorly understood.

We examine the seasonal (April–September) and the interannual (for late summer/early fall) variability of the temperature (T) and salinity (S) fields, employing both recently collected and historical data. The data allow a spatially broad and integrative analysis that permits us to quantify sources and sinks for freshwater content (FWC) and heat content (HC) and to identify advective effects that impact coastal and mid-shelf water mass exchanges. We will show that the processes resulting in thermal and haline interannual variability are largely uncoupled from one another both seasonally and mechanistically. Although we emphasize physical processes, the results likely bear on shelf nutrient distributions and biological productivity. For example, exchanges that introduce low-salinity (<31) and nitrate-poor (Fig. 2) inshore waters onto the central shelf may inhibit primary production.

The Bering Sea shelf is vast: its cross-shelf extent is 800 km between the mouth of Norton Sound and the continental slope, and the shelfbreak extends 1200 km northwestward from Unimak Pass to Cape Navarin. The slope is incised by several canyons (Navarin, Pervenets, Pribilof, Bering, and Zhemchug), all likely playing an important role in shelf/basin exchange (Schumacher and Reed, 1992; Stabeno and Van Meurs, 1999; Mizobata and Saitoh, 2004). Our focus here is on the shallower waters on the mid- and inner-shelf.

Previous studies (Kinder and Schumacher, 1981b; Coachman, 1986) discuss the outer (100–200 m), middle (50–100 m), and coastal (0–50 m) biophysical domains of the southeastern Bering

* Corresponding author. Tel.: +1 907 474 7834; fax: +1 907 474 7204.
E-mail address: seth@ims.uaf.edu (S. Danielson).

0278-4343/$ - see front matter © 2010 Elsevier Ltd. All rights reserved.
doi:10.1016/j.csr.2010.12.010

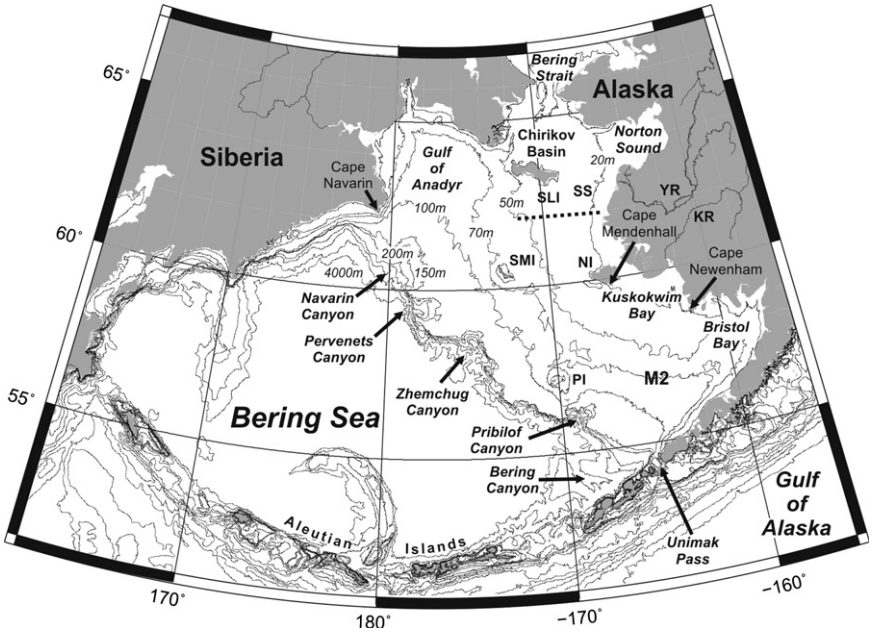

Fig. 1. Map of the Bering Sea labeled with place and feature names employed in the text. Abbreviations denote: YR=Yukon River; KR=Kuskokwim River; SS=Shpanberg Strait; SLI=St. Lawrence Island; SMI=St. Matthew Island; PI=Pribilof Islands; NI=Nunivak Island. M2 denotes the site of NOAA Mooring 2 on the 70 m isobath. The CTD transect of July 2009 is denoted by a dotted line along 62°N. The Arctic Ocean lies to the north of Bering Strait and the greater Pacific Ocean lies south of the Aleutian Islands. Depth contours are plotted at the following depth levels: 20, 50, 70, 100, 150, 200, 500, 1000, 2000, 3000, 4000, 5000, and 6000 m.

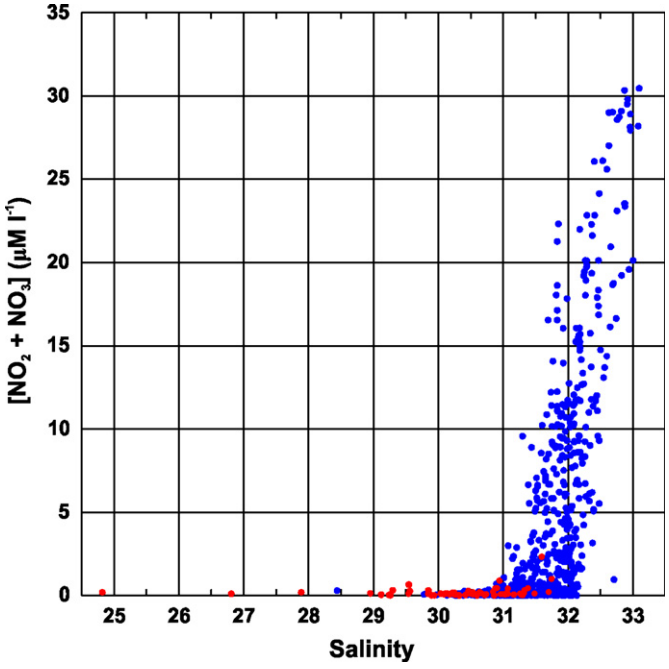

Fig. 2. Relation of total nitrate to salinity for 779 water samples collected across the Bering Shelf between 2002 and 2006. Red (blue) points denote stations where the total water depth is less than or equal to (greater than) 30 m.

Sea shelf. The northern limit of these domains is not well described, but Coachman (1986) notes that the inner-front, which marks the boundary between the coastal and middle domains, separates from the 50 m isobath north of Nunivak Island. Due to the distribution of available conductivity-temperature-depth (CTD) data (Fig. 3), we focus on the region that overlaps both the middle and coastal domains and which extends from western Bristol Bay to south of St. Lawrence Island. In particular, we consider the part of the central Bering Sea shelf lying (1) west of 162°W; (2) east of 174°W; (3) north of 57°N; (4) south of 62.5°N; and (5) between the 20 and 70 m isobaths (delineated in Fig. 3). This region forms our integration domain and represents the maximum area common to CTD surveys conducted annually from 2002 to 2007. It encompasses $\sim 2.07 \times 10^5$ km^2 with a mean water depth of 45 m and a volume of $\sim 9.3 \times 10^3$ km^3. For comparison, the entire shelf has an area of 1.8×10^6 km^2, a mean depth of 43 m, and a volume of 7.7×10^4 km^3 between the 100 m isobath and the coast.

In assessing causes of anomalies in HC and FWC we examine integrated surface heat fluxes, ice extent and melting, river discharge, precipitation (P) and evaporation (E), sea level pressure, winds, and ocean currents. Although mean currents are typically small (1–5 cm s^{-1}; Schumacher and Kinder, 1983; Danielson et al., 2006), we show that wind-forced advection of both heat and freshwater are nevertheless important and are associated with variations in the seasonal position and strength of the Aleutian Low. The Aleutian Low influences the cloud cover (Reed, 1978), wind mixing (Overland et al., 2002), and heat fluxes, as well as the wind stresses that advect water (Bond et al., 1994) and ice (Overland and Pease, 1982).

On this shelf, both temperature and salinity affect the location and strength of fronts and of the pycnocline (Kinder and Schumacher, 1981a), across which nutrient fluxes influence summer primary production (Sambrotto et al., 2008; Bond and Overland, 2005). The annual evolution of the temperature and salinity fields is as follows. North of ~60°N, the water column is reset to the freezing point (~ −1.8 °C) by the end of each winter (annual HC minimum), coincident with the annual shelf salinity maximum (annual FWC minimum; Schumacher et al., 1983). Winter ice extent is variable, since it depends upon both local ice formation and southward advection by winds (Muench and Ahlnas, 1976; McNutt, 1981), but ice occasionally extends as far as the Alaska Peninsula (Niebauer and Schell, 1993). Throughout winter, ice melts continually along its southernmost boundary (Pease, 1981). Rapid ablation from the seasonal increase in solar radiation occurs in May, while the southerly winds (Niebauer et al., 1999) advect thinning ice northward (Overland and Pease, 1982).

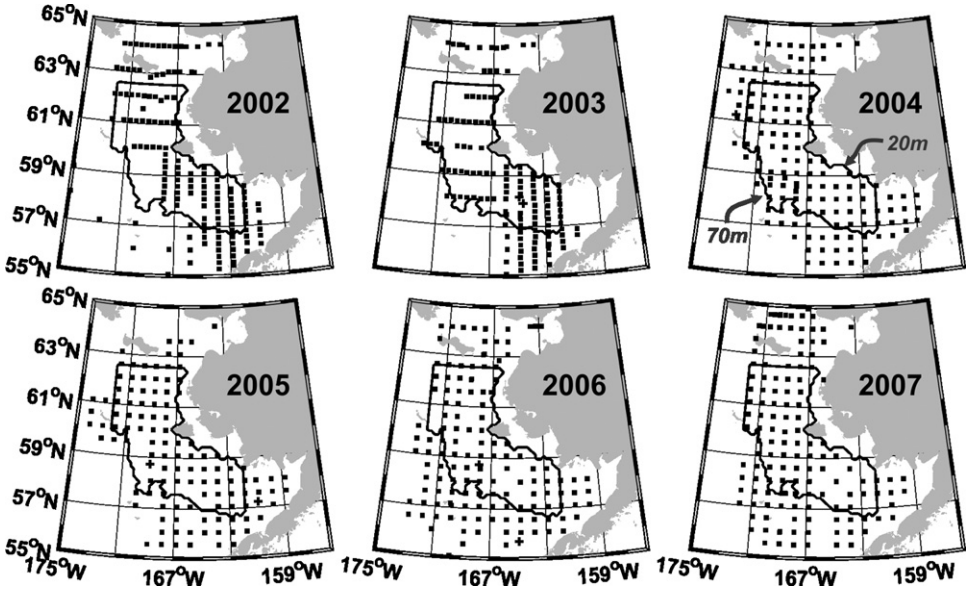

Fig. 3. 2002–2007 CTD station coverage over the eastern Bering Sea shelf. The region that bounds heat and freshwater integrations is denoted in each panel by a contour line. Dots show locations of good temperature and salinity data; plus signs show locations of good temperature data only. Nominal station spacing of ½° latitude (56 km) is achieved in 2004–2007 across most of the focus domain; west of Nunivak Island in 2002 and 2003 the station spacing is 1° of latitude, or about 111 km.

Table 1
Summary of the 2002–2007 BASIS CTD survey timing and coverage and spring environmental conditions.

Year	Number of CTD stations	CTD survey start date	CTD survey end date	Date of maximum ice extent	Date of ice retreat	March/April mean ice extent (km^2)	Heating season onset (170°W, 60°N)
2002	154	20 Aug	7 Oct	20 Feb	18 May	52 000	4 Apr
2003	129	21 Aug	8 Oct	26 Mar	6 May	51 000	9 Apr
2004	143	14 Aug	30 Sep	2 Apr	11 May	65 000	6 Apr
2005	128	14 Aug	6 Oct	9 Apr	21 May	62 000	21 Apr
2006	137	17 Aug	20 Sep	4 Feb	31 May	88 000	29 Apr
2007	166	15 Aug	8 Oct	24 Mar	24 May	101 000	20 Apr

The number of CTDs reported reflects only those taken over the eastern Bering Sea shelf. The date of maximum ice extent and mean retreat date are computed for the greater eastern Bering Sea shelf area, while the ice extent column is given for the central region only. A 5-day moving average window was applied to the net surface heat flux time series to estimate the heating season onset date.

Melting and warming then initiate the water column stability required for the spring phytoplankton bloom (Alexander and Niebauer, 1981; Stabeno et al., 2001). Solar heating through spring and summer further strengthens the thermal stratification (Reed and Stabeno, 2002). Hence, mid-shelf waters evolve toward a strongly stratified two-layer system, maintained primarily by wind mixing and solar heating in the surface layer and tidal mixing of cold winter water in the lower layer (Coachman, 1986; Overland et al., 1999).

Here we present CTD data from 2002 to 2007, collected over the shelf between mid-August and early October of each year as part of the U.S. Bering–Aleutian Salmon International Survey (BASIS) program (Fig. 3 and Table 1). Observations include physical and chemical data, as well as phytoplankton, zooplankton and fisheries sampling. The primary goal of BASIS is to understand the effects of climate change and climate variability on the pelagic ecosystem of the eastern Bering Sea. The fisheries and oceanographic data are employed to reduce uncertainty in forecasting groundfish and western Alaska salmon populations. The survey grid achieves unprecedented CTD coverage. Although the sampling is not synoptic (40–60 days per year are required), we will show that the surveys span the period when both the FWC and HC of the shelf waters are at their annual maxima, and that interannual variability in FWC and HC is not obscured by seasonal or synoptic variability.

We also employ both recently collected (2007–2009) CTD data from the Bering Sea Ecosystem Study (BEST) and historical CTD data (1929–2009) from the National Ocean Data Center (NODC) World Ocean Database 2009 (WOD-09) (Boyer et al., 2009) to evaluate seasonal changes in FWC and HC.

Section 2 contains detailed descriptions of the data and their processing. In Section 3 we present the mean and variability of the late summer/early fall T and S fields and investigate spatial correlations in T and S anomalies. Upon integrating across the central shelf region, we relate the seasonal and interannual anomalies in FWC and HC to direct flux estimates and to indirect measures of oceanic advection (Section 4). Section 5 summarizes the key results and discusses implications of the analyses.

2. Data sets and methods

2.1. CTD data

The BASIS CTD data were collected with a variety of Sea-Bird Electronics (SBE) CTDs over the years: SBE-19 and SBE-19+ (2002), SBE-25 (2003, 2004, and 2005), SBE-917 (2005–2007), and SBE-911 (2005–2007). Instruments were calibrated prior to each season, and 2004–2006 salinity measurements were compared to discrete

bottle samples. The CTD profiles were processed using the SBE data processing subroutines (SBE, 2009), and final data were binned to 1-m depths and inspected for spikes and/or spurious density inversions. Measurement spikes exceeding ~0.01 were removed by linearly interpolating through adjacent depth levels. Based on post-calibrations, comparison with secondary probes, and discrete salinity samples, we consider the accuracy of the temperatures to be better than 0.01 °C and salinities better than 0.02. Because there are year-to-year differences in station spacing and sampling grids, we linearly interpolated the temperature and salinity data to regular 2- and 3-dimensional grids to ensure consistency in subsequent calculations. The CTD data from the BEST cruises of 2007, 2008, and 2009 (HLY0701, HLY0802, HLY0803, HLY0901, KN19510, and PS0909) were collected with SBE-911 instruments and processed and evaluated following procedures similar to those applied to the BASIS CTD data.

Historical CTD and bottle data from the NODC WOD-09 (Boyer et al., 2009) were screened for position errors (samples appearing on land and deep samples from a site known to be shallow) and anomalous temperatures and salinities. Questionable values and outliers, defined in part by the binning method described below, were discarded.

Combining the various data, we formed 0–100 m monthly and seasonal vertical profiles across a regular geographic grid with spacing of one degree of latitude and two degrees of longitude. The BASIS sampling occurs between August and October (late summer to early fall); it coincides with the annual FWC and HC maxima. February–April (late winter to mid-spring) represents the annual FWC and HC minima and May–July (late spring to mid-summer) encompasses the transition from late spring to late summer. Linear interpolation between depths at stations with discrete bottle samples created full water column profiles. In order to avoid biasing the gridded results toward years with more CTD casts, data were first reduced into a single representative profile for each grid cell, year and month. The monthly profiles were then averaged into a single mean monthly profile representing each grid cell.

Twenty of the grid cells are more than 50% contained within our integration domain (Fig. 3), and for these 20 cells data were collected in 16–48 discrete years in May–July and 18–33 years in August–October. We place a moderate to high level of confidence in results derived from these data. During February–April one cell was sampled in only 2 years, while the remaining 19 cells were sampled in 4–23 years. We ascribe low to moderate confidence in these results. For November–January the data distribution was too sparse to be useful, so we neglect this period.

2.2. Mooring data

Temperature and salinity data from NOAA mooring M2 (56.9°N, 164.1°W) (Stabeno, unpublished data) and collected between 1995 and 2006 near 10 and 60 m are used to assess seasonal HC and FWC changes, and to estimate the probable end-of-winter water column HC. Data were inspected for spikes and consistency with other nearby measurements on the mooring line. Suspect data were discarded, and the resultant data set was averaged into monthly mean values.

2.3. Nutrient data

Nitrate plus nitrite concentrations were determined from discrete water samples collected using Niskin bottles attached to the CTD. Whole water samples were stored frozen at −20 °C and analyzed within 8 months at the University of Washington Marine Chemistry Laboratory using colorimetric protocols (UNESCO, 1994).

2.4. Ice cover data

Ice cover data are obtained from the National Snow and Ice Data Center (NSIDC) passive microwave satellite Level 3 archives (Comiso, 1999), available on a 25 km grid. Data from 1988 to the present are daily, while data from 1979 to 1987 were collected every other day. We estimate the number of ice-free days by employing a concentration-extent time series computed over the region south of 66°N (Bering Strait) and east of 170°E (Cape Navarin). Ice decay and growth occur relatively rapidly and extensively, and so we employ a fixed ice concentration-extent threshold (5×10^4 km^2) to determine the onset of the open water and ice-covered seasons. For comparison, the area of Norton Sound encompasses approximately 5×10^4 km^2. Experiments indicate that our results are relatively insensitive to the threshold value.

2.5. Streamflow data

Daily discharge data were obtained from the U.S. Geological Survey streamflow database (http://waterdata.usgs.gov/nwis) for the Yukon and Kuskokwim rivers at Pilot Station and near Crooked Creek, respectively. Data gaps were filled with the mean daily climatological value.

2.6. Drifter data

Satellite-tracked oceanographic drifter data are employed to examine nearshore and mid-shelf surface advection in the summer and fall. Fifteen drifters were deployed in 2002 and 32 were deployed in each of 2008 and 2009. Seventy of these were CODE surface drifters drogued at 1 m depth (Davis, 1985) and the remaining nine drifters (2002 deployment only) had holey sock drogues centered at 10 m depth. The drifters acquire GPS position fixes (measured on a beached drifter to be accurate to ~20 m) every 30 or 60 min. After inspection for faulty position or time fixes, the data are converted into velocities and gridded onto 1/2° latitude by 1° longitude cells. To avoid tidal aliasing, only cells that contain at least 5 drifter-days (120 h) are used.

2.7. St. Paul meteorological data

Daily precipitation data collected at St. Paul Island and obtained from the National Climate Data Center are scaled by the central shelf area to estimate precipitation fluxes within our integration domain. Long-term mean monthly precipitation records from coastal meteorological stations at Nunivak Island, Cape Newenham, St. Lawrence Island, and Nome show that the St. Paul values are within +60% and −120% for the April–September integration period and ±70% for October–May. The average difference between St. Paul and the other stations for these two time periods is 2% and 23%, respectively.

2.8. Sea surface temperature data

The Smith et al. (2008) Extended Reconstructed Sea Surface Temperature (ERSST) data set, version ERSST.v3, is employed to assess the late winter distribution of surface temperatures. The ERSST data, gridded monthly onto a 2° global grid, are constructed from a temporal–spatial interpolation scheme applied to the International Comprehensive Ocean–Atmosphere Data Set (ICOADS) sea surface temperature data. To gain a relative measure of the accuracy of this product in our region, we compare the ERSST data to the near-surface (~10 m depth) temperature record from the NOAA M2 mooring. We find the ERSST has an offset of +0.54 °C, which may be explained by the difference in depth levels. Monthly

anomaly standard deviations are 0.76 and 1.2 °C for the ERSST and M2 data, respectively. The ERSST monthly anomalies account for 35% of the variability observed at M2: $r=0.59$ and $p=0$.

2.9. Atmospheric model fields

Winds, surface pressures, and surface heat fluxes are taken from the NCEP/NCAR Reanalysis Project 1 (NCEPR; Kalnay et al., 1996). We use this product rather than Reanalysis 2 output fields because the model performance summaries described below were developed for the NCEPR results, and the model run extends further back in time. The NCEPR consists of 6-hourly hind casts of major atmospheric variables on an ~2.5° global grid from 1948 to the present. Monthly output fields are employed for retrospective analyses and six-hourly fields for comparison to the BASIS records.

The net surface heat flux is the sum of the net shortwave, net longwave, latent, and sensible heat fluxes. The NCEPR model surface heat flux performance varies around the globe (e.g., Weller et al., 1998; Rouault et al., 2003), but typical evaluations indicate net shortwave root-mean-square (RMS) errors of 30–70 W m^{-2} and biases of up to 40 W m^{-2} (Taylor, 2000; Scott and Alexander, 1999). Sensible and latent heat fluxes have RMS errors and mean biases of 6 and 20 W m^{-2}, respectively, when compared to ship-based measurements (Smith et al., 2001). While a constant bias will not affect the results of our anomaly analysis, it will impact our estimates of the seasonal heat flux. For the southeast Bering Sea, Ladd and Bond (2002) find that the NCEPR overestimates the shortwave radiation flux by 50–70 W m^{-2} in summer, and they ascribe the discrepancy to the model's inability to simulate low clouds and fog. Reed and Stabeno (2002) computed the surface heat fluxes at the NOAA mooring site M2 for 3 months in the summer of 1996. In comparing their results to the NCEPR monthly mean heat fluxes, we find that for May, June, and July 1996 the NCEPR had mean biases of +36, −33, +3, and +5 W m^{-2} for the shortwave, longwave, latent, and sensible heat fluxes, respectively. The biases in the shortwave and longwave terms nearly balance, resulting in a total bias of +11 W m^{-2}, or ~4% of the net surface heat flux in summer. We take this value to be representative of the net surface heat flux error for the NCEPR over the Bering Sea in summer, and we therefore reduce the NCEPR net surface heat flux computations by this same amount.

Although Smith et al. (2001) find an NCEPR underestimate of near-surface wind speeds of ~2–3 m s^{-1}, Ladd and Bond (2002) find good agreement between the winds recorded at the NOAA surface mooring M2 and the NCEPR wind vectors, and so no speed correction has been applied to the model winds.

2.10. HC and FWC computations

The oceanic HC and FWC computations are described by Eqs. (1) and (2):

$$HC = \iiint C_p(x,y,z)\rho(x,y,z)[T(x,y,z)-T_r]\,dx\,dy\,dz, \quad (1)$$

$$FWC = \iiint \frac{\overline{S}-S(x,y,z)}{\overline{S}}\,dx\,dy\,dz, \quad (2)$$

where C_p is the heat capacity, ρ is the density, $T_r=0$ is the arbitrary reference temperature, and $\overline{S}=31.5$ (the arbitrary reference salinity) is the mean salinity for the BASIS data within our integration domain. Anomalies in seasonal and interannual HC and FWC are calculated as differences between the observed values and the annual or multi-year means, respectively, and they reflect the actual amount of heat and FW required to transform the volume considered from the mean state to that observed. Other reference salinities lead to different (and larger) FWC, but the relative fluctuations from year to year and season to season remain essentially the same, with the sensitivity to reasonable choices in *reference salinity* being slight (~3% difference in anomaly for a change of 1 in salinity). Our goal is to examine the variability in HC and FWC, not the standing stock, and this is readily accomplished with the reference values chosen.

To provide the simplest overall picture of interannual and seasonal changes, we integrate over the largest region common to the multi-year BASIS CTD grid, rather than further dividing the shelf into still smaller subdomains. One limitation of this data set is that no BASIS samples are taken from waters shallower than 20 m depth, which in places can be 100 km from the coast, and so the sampling does not resolve the coastal jet well (Fig. 11, based on BEST data, shows this feature clearly). The vast majority of the shelf water volume sits over bottom depths > 30 m, however, and so the integrations reflect overall shelf conditions reasonably well.

3. Results

This section provides a detailed examination of the late summer/early fall (August–October) shelf conditions as depicted by the BASIS data. We first examine the mean conditions (Section 3.1) and then variability about the mean (Section 3.2).

3.1. Late summer/early fall mean T and S fields

We compute the mean T and S distributions for 2002–2007 above and below the MLD, with the MLD defined as the depth where σ_t is 0.10 kg m^{-3} greater than the value at 5 m depth.

The panels in Fig. 4 show T and S fields that differ substantially with respect to the along-isobath direction. Below the MLD, horizontal temperature gradients are generally cross-isobath, and the "cold pool" tongue (winter-formed waters with temperatures < 2 °C; Takenouti and Ohtani, 1974) extends southeastward, centered on the 70 m isobath. Above the MLD, temperature gradients south of 60°N are primarily along-isobath, whereas north of 60°N these gradients are chiefly cross-isobath. For waters < 30 m deep, the warm tongue that extends northwestward toward Nunivak Island suggests the presence of a front and associated jet, for which we present additional evidence below.

In contrast to the temperature field, salinity gradients are generally oriented in the cross-isobath direction both above and below the MLD. Therefore, in the along-isobath direction, advection will play a different role in setting the heat and freshwater budgets at the end of summer. For example, for waters south of 60°N and above the MLD, where the along-shelf temperature gradient is ~1 °C per 100 km, along-isobath advection will not affect the salt budget, but will impact the heat budget.

As previously observed by Takenouti and Ohtani (1974) and Coachman (1986), we find that isohalines cross the isobaths west and north of Nunivak Island, first directed NW offshore of the 30 m isobath and then turning NE toward Norton Sound. The latter turning reflects the influence of the eastward flow south of St. Lawrence Island that carries relatively dense water from the Gulf of Anadyr (Schumacher et al., 1983; Danielson et al., 2006). This saline water, along with the fresher coastal waters adjacent to the Alaskan mainland, flows northward through Shpanberg Strait, where the largest horizontal density gradients are found. The westward bulge of low salinity water centered along 61°N may consist in part of water from the Yukon and Kuskokwim, but also of other low-salinity coastal waters advected from farther south.

The relative position of the 31 isohaline above and below the MLD reflects the combined effects of stratification, advection, and mixing as mid-shelf and coastal waters flow northward. Offshore of Cape Newenham, the near-bottom 31 isohaline is directed approximately

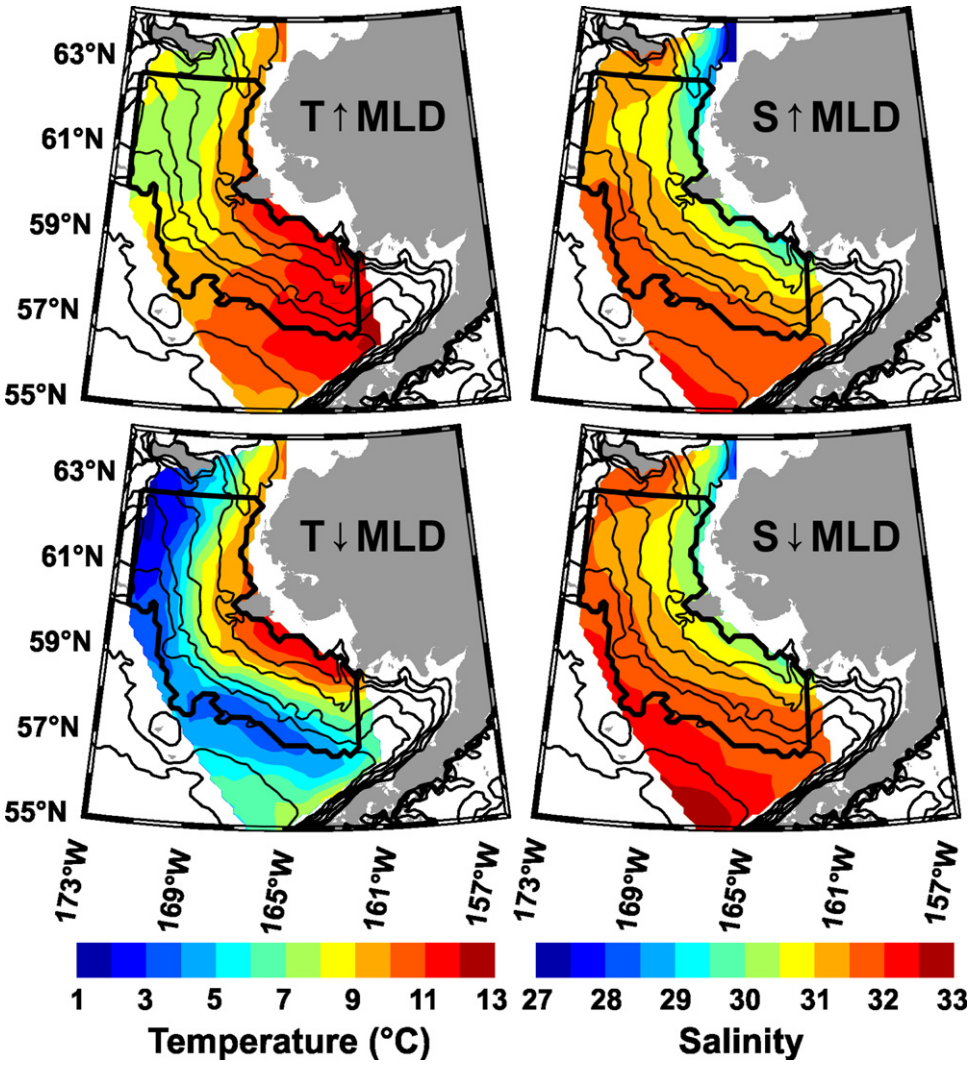

Fig. 4. Mean late summer–early fall 2002–2007 distributions of temperature (left) and salinity (right) above (top) and below (bottom) the mixed layer depth. The region that bounds heat and freshwater integrations is denoted in each panel by a thick contour line. Depth contours are plotted at the following levels: 20, 30, 40, 50, 60, 70, 100 and 200 m.

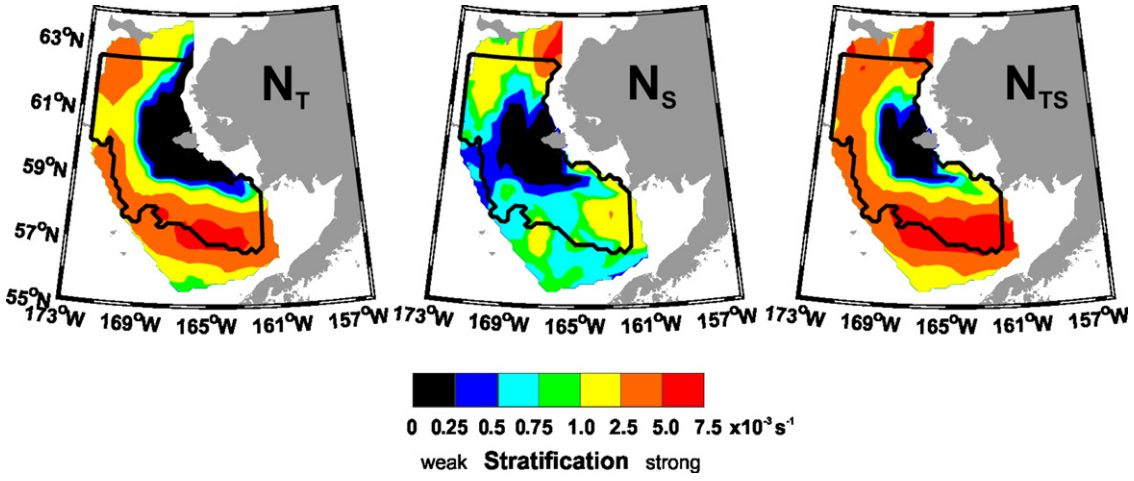

Fig. 5. 2002–2007 mean maximum water column Brunt–Vaisala frequency computed by holding the salinity constant at the water column mean (left); by holding the temperature constant (center); and by allowing both temperature and salinity to vary (right). Note the nonlinear color scale.

WNW. Above the MLD, it is directed NW, and the distance between the surface and bottom 31 isohalines exceeds 100 km. Near 60°N, the locations of this isohaline at the surface and at the bottom converge, indicating that the water column is nearly homogeneous in salinity (also see Fig. 5). North of 60°N, the isohalines diverge again as the fresh surface waters presumably spread offshore.

Strong thermal stratification ($N_T^2 > 1 \times 10^{-3}$) develops in summer in waters seaward of the inner-front, and the stratification is a maximum along the 70 m isobath, coincident with the "cold pool" tongue extending from the NW (Fig. 5). Inshore of the inner-front, the water column is only weakly stratified thermally. In contrast, strong salt stratification occurs near the Yukon River plume, south of St. Lawrence Island, and in western Bristol Bay. Within the extensive region between about 58°N and 61°N, however, the salinity contribution to stratification is minimal ($N_S^2 < 0.5 \times 10^{-3}$), suggesting that low-salinity coastal waters do not penetrate offshore at this time of the year.

Evaluating volumetric *T*–*S* contributions over the 0–20 m depth range (46% of the central shelf volume), we find that temperatures range between 5 and 14 °C and salinities between 28 and 32.5. Major volumetric *T*–*S* modes are centered at (~6 °C, 31) and (~8 °C, 31), and a smaller third peak is at (12 °C, 31.5). These modal peaks primarily represent low-nitrate waters, since concentrations of (NO_3+NO_2) are 0–1 μM for salinities < 31 (Fig. 2). For the 0–20, 21–40, and 41–70 m depth levels, the mean observed (NO_3+NO_2) concentrations are 0.5, 3.8, and 7.0 μM, respectively. The 41–70 m depth range (18% of the central shelf volume) consists of one dominant *T*–*S* volumetric mode (4 °C, 32) and one secondary mode (0 °C, 31.5). The deep salinities vary narrowly (31–33) and temperatures are mainly between −2 and 6 °C. Mid-depth waters (36% of the central shelf volume) occupy nearly the entire range of temperatures encompassed by the surface and bottom layers (−2 to 12 °C) but cover only a portion of the salinity range (30–32.5). At the end of summer, waters colder than 2 °C are geographically isolated from waters with salinity < ~30 since the former are offshore and deep while the latter are nearshore and shallow.

3.2. Interannual variability of the late summer/early fall T and S fields

The late summer/early fall 2002–2007 annual anomalies above and below the MLD, referenced to the 2002–2007 means (Fig. 4), are mapped in Fig. 6. Strong positive and negative temperature or salinity anomalies can occur in the same year, and they can encompass areas of 2×10^4 km^2 or more. Hence, classifying a particular year as "warm" or "fresh" can be misleading, since one portion of the shelf may be anomalously warm while another is anomalously cold. The anomaly maps further show that: (1) salinity anomalies are sometimes out of phase between the inner- and middle-shelf; (2) interannual variability in the thermal and haline contributions to stratification is relatively large and spatially variable; (3) boundaries between positive and negative anomalies

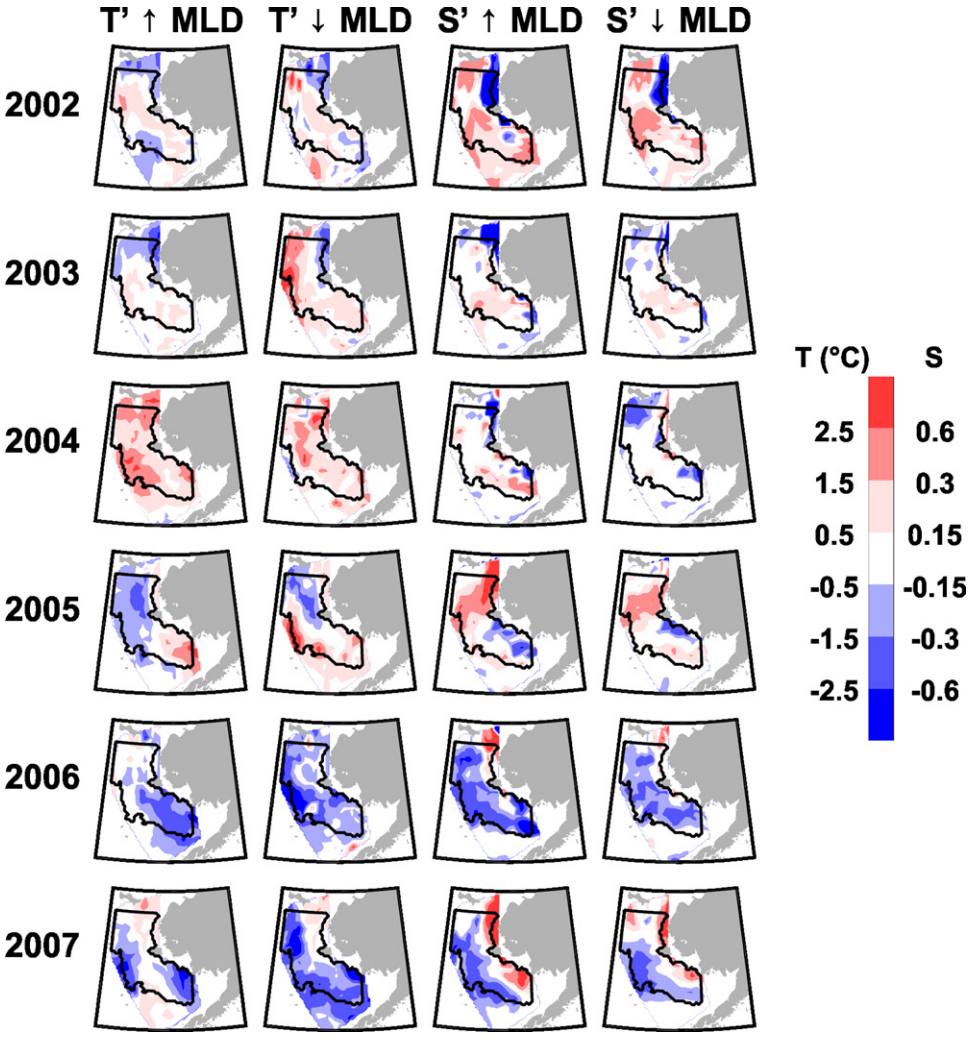

Fig. 6. Temperature and salinity anomalies above (↑) and below (↓) the mixed layer depth (MLD=depth where $\sigma_t = \sigma_t$ at 5 m+0.1 kg m^{-3}). Anomalies are computed in temperature and salinity units with respect to the multi-year means shown in Fig. 4. Blue (red) colors indicate that the temperature/salinity anomalies are warmer/saltier (cooler/fresher) than the mean fields. The region that bounds heat and freshwater integrations is denoted in each panel by a thick contour line.

generally coincide with bio-physical domain boundaries such as the inner-front, although this was not the case in 2005 (e.g., for temperatures below the MLD); (4) waters north of Nunivak Island were fresh in 2002; (5) 2004 was a warm year both above and below the MLD; (6) extensive regions of both cold and warm anomalies occurred in 2005; and (7) 2006 and 2007 were cold and fresh below the MLD except on the inner-shelf and north of Nunivak Island in 2007.

Figs. 7 and 8 are correlation maps of the anomalies. (For Pearson's correlation coefficient r with N independent samples, the appropriate number of degrees freedom is $N-2$. With $N=6$ years of data, statistical significance at the 95% confidence level occurs for $|r| \geq 0.81$; Mendenhall and Sincich, 1988.) Fig. 7A shows the correlation at each grid point between the temperature anomalies above and below the MLD for 2002–2007. Significant vertical temperature correlations are restricted to well-mixed waters within and inshore of the inner-front. Elsewhere the correlations are generally weak, implying little communication between the upper and lower waters after stratification sets up. In contrast, salinity is significantly correlated and in phase above and below the MLD over most of the region (Fig. 7B), suggesting that whatever process sets the shelf salinity anomalies operates during the time of year when the water column is well mixed.

Fig. 8 depicts horizontal structure in the temperature and salinity anomalies both above and below the MLD, mapping the correlation between the anomaly at each of four reference points (near Cape Newenham, near NOAA mooring M2, south of St. Lawrence Island, and offshore of the Yukon River) with the anomaly at all other grid points in the domain. The reference points are chosen to represent nearshore, offshore, southern and northern regions of the domain. The nearshore reference points are located close to the Yukon and Kuskokwim river discharge points. We observe that (1) the correlation scales are much broader than the station spacing, hence the BASIS sampling sufficiently resolves interannual anomalies; (2) the de-correlation length scale for temperature anomalies generally exceeds that of the salinity anomalies in the southern portion of the domain, suggesting that different processes control the spatial variability of temperature and salinity; (3) the temperature de-correlation length scale in the southern portion of the domain (200–500 km) is greater than in the north (100–200 km); (4) correlated temperature anomalies span coastal and mid-shelf regions in both the south and the north; and (5) salinity is generally anti-correlated between the nearshore and mid-shelf regions, although the statistically significant extent of the anti-correlations is limited.

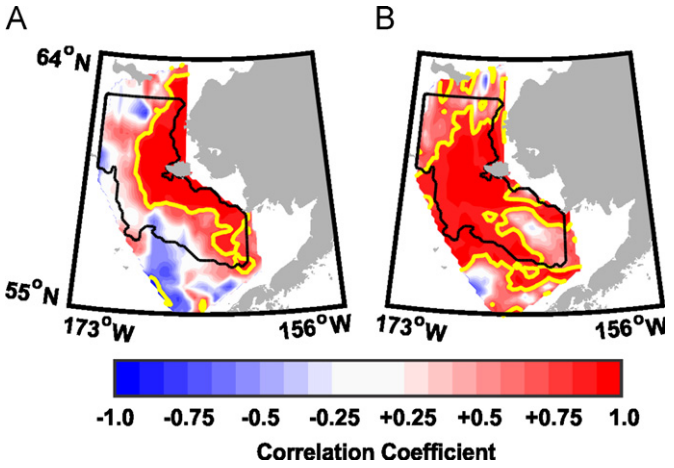

Fig. 7. Late summer–early fall temperature (A) and salinity (B) vertical correlation maps, showing the temporal correlation between values above the MLD with values below the MLD at zero lag. Red indicates positive correlation; blue indicates negative. Yellow contours denote significance at the 95% confidence level ($r = \pm 0.81$). The region that bounds heat and freshwater integrations is denoted in each panel by a black contour line.

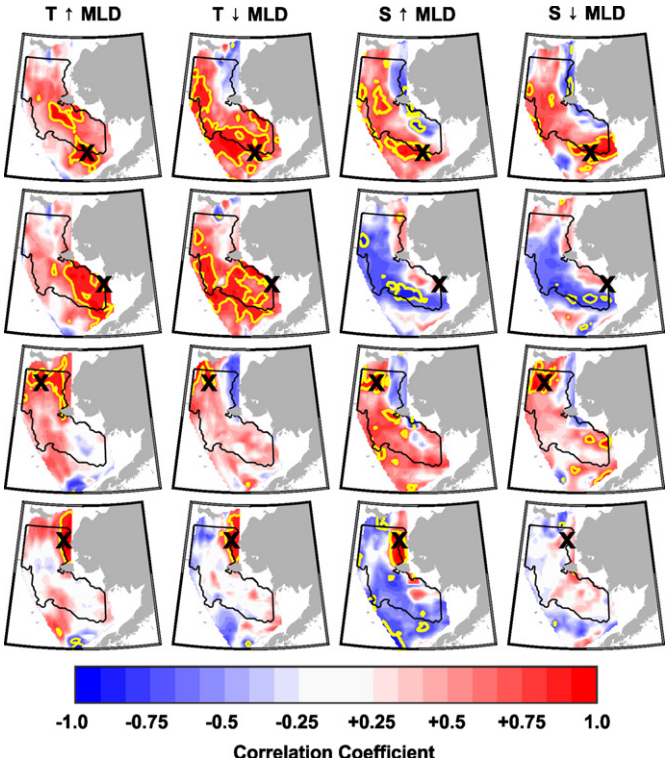

Fig. 8. Late summer–early fall temperature and salinity horizontal correlation maps; color scheme and map bounds are as given in Fig. 7. Correlations are computed at between the point marked by an "X" on each panel and all other grid points for each column from left to right as marked: temperatures above the MLD; temperatures below the MLD; salinity above the MLD; and salinity below the MLD.

4. Freshwater and heat content variability and fluxes

In this section we investigate seasonal (Section 4.1 and Figs. 9 and 10) and interannual (Sections 4.2–4.3 and Tables 2 and 3) variability in FWC and HC parameters. Subsequent scaling arguments, dynamical considerations, and flux estimates will allow us to examine possible advective contributions to the heat and salt budgets.

4.1. Seasonal variability

We place the late summer/early fall period described above within a seasonal context by compiling quarterly depth-averaged means of the 0–100 m temperature and salinity fields across the eastern Bering Sea using the historical, the BEST, and the BASIS CTD data (Fig. 9).

Late winter/early spring (February–April) is characterized by near-freezing temperatures north of 60°N and a high-salinity pool north of 62°N. The salty waters surrounding St. Lawrence Island reflect winter ice formation and the eastward advection of Anadyr waters (Schumacher et al., 1983; Drucker et al., 2003; Danielson et al., 2006). While the saline water found between Nunivak and St. Lawrence islands might be an artifact of the small sample size, it more likely results from locally produced brine because Danielson et al. (2006) did not observe southerly fluxes of dense water from the St. Lawrence Island region and the sample size on the southern end of this feature is not small.

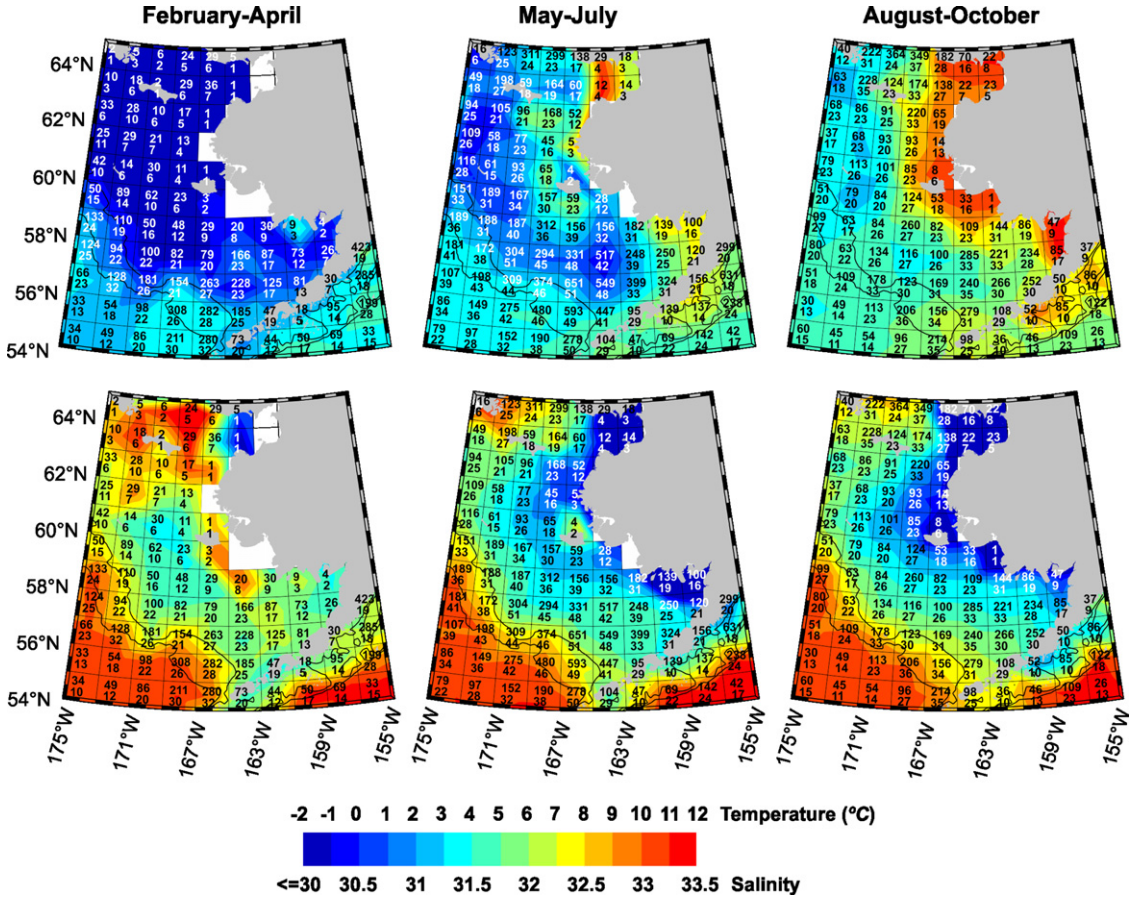

Fig. 9. Climatology of the 0–100 m mean temperature (top row) and salinity (bottom row) in the eastern Bering Sea during the time periods indicated. The upper number in each grid cell indicates the total number of casts for the cell; the lower number denotes the number of years represented by these casts. Note the existence of some cells with no or few data points.

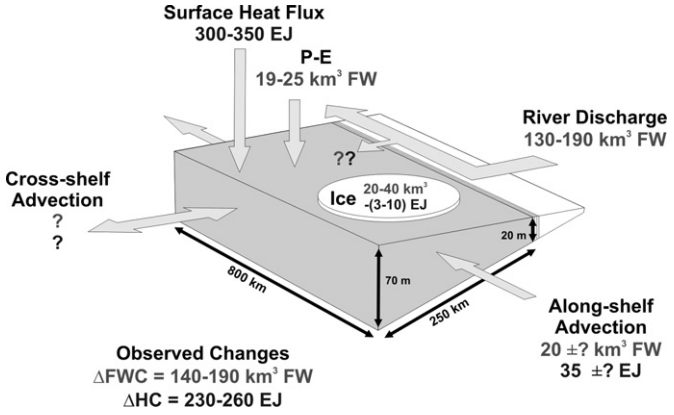

Fig. 10. April–September estimated fresh water (FW) and heat fluxes and changes in standing stocks for the central Bering Sea shelf. 1 EJ = 10^{18} J. Question marks denote unknown fluxes.

Table 2
Annual anomalies of the 2002–2007 summer's end FWC, mean FWC of sea ice (March–April mean), FWC of the May–August $P-E$, FWC of the March–August Yukon and Kuskokwim discharge, and the preceding October–May cross-isobath Ekman transport.

Year	Summer's end FWC (km^3)	Ice FWC (km^3)	$P-E$ (km^3)	River discharge (km^3)	Cross-shore Ekman transport ($\times 103\ m^3\ s^{-1}$)
2002	−51	−7.4	−1.6	−11	35.9
2003	−13	−7.1	2.9	−9	1.58
2004	2	−1.5	−2.2	−4	5.08
2005	−45	−2.5	−1.8	38	103
2006	77	6.7	−1.1	6.4	−98.7
2007	31	11.8	3.7	−5.4	−46.4
σ	48.3	7.7	2.5	18.4	
r		0.78	0.24	0.16	**−0.93**
p		0.065	0.65	0.76	**0.0072**

The bottom three rows show standard deviation (σ), correlation coefficients (r), and p-values (p) for the anomalies. The correlation and p-values summarize cross-correlation computations between column 2 and columns 3–5. Correlations significant at the 95% level are highlighted in boldface type.

A pool of relatively fresh water extends northward between St. Matthew Island and Nunivak Island. This water may be coastal water remnant from the previous fall (see later Section 5) and/or melt waters from the ice pack edge. Low salinity observations ($S<31$) in Norton Sound at the end of winter are difficult to evaluate: they are comprised of only 1 year sampled in each of two grid cells. While these measurements may not be representative, we note that previous drifter deployments suggest that the residence time of near-surface waters within Norton Sound may be many months (T. Weingartner, unpublished data; see also http://www.ims.uaf.edu/drifters/), and so these observations may in fact reflect over-wintered Yukon discharge.

By late spring and mid-summer (May–July), waters begin warming in shallow coastal waters along the Alaskan Peninsula and in Norton Sound. Relatively fresh (<31) coastal water envelopes the entire coast north of eastern Bristol Bay as river

Table 3
Annual anomalies of the 2002–2007 summer's end oceanic HC, winter's end oceanic HC, April–August net surface heat flux and April–August along-isobath Ekman transport.

Year	Summer's end HC (EJ)	Winter's end HC (EJ)	April–August surface heat flux (EJ)	April–August along–isobath Ekman transport ($\times 10^3$ m^3 s^{-1})
2002	12.0	23	9	5.9
2003	28.0	14	6	7
2004	45.0	1	13	35
2005	3.0	−9	−7	−8.5
2006	−42.0	−22	−15	−32
2007	−47.0	−7	−6	−7.5
σ	36.5	16.4	11.0	
r		0.64	**0.86**	**0.85**
p		0.175	**0.027**	**0.032**

Table layout is as described for Table 2. 1 EJ = 10^{18} J.

discharge increases. Though not resolved in the 3-month mean, in July a salty tongue protrudes onto the shelf near Zhemchug canyon, likely a mid-summer source of high-nitrate waters to the outer- and middle-shelf. The appearance of this intrusion coincides with the seasonal relaxation of the Aleutian Low and the associated cyclonic wind stress across the Bering Sea basin (Brower et al., 1988), and the intrusion may reflect the interaction of the canyon with the adjustment of the shelfbreak front to changing winds (Gawarkiewicz and Chapman, 1992; Chapman and Lentz, 1994, 1997).

By late summer/early fall (August–October) the central shelf's annual HC and FWC are both maximum (although we do not have data from November to January).

We next use the 0–100 m gridded CTD data to compute quarterly and monthly FWC and HC anomalies on the central shelf, and we show in Fig. 10 the magnitude of their seasonal changes between April and September, along with the dominant flux terms. A measure of sensitivity to the choice of base climatology is gained by comparing changes in HC and FWC from using the 2005 version of the WOD (Boyer et al., 2006), instead of WOD-09 and excluding the BEST data. We find that the integrated HC estimates change by less than 15%, but the integrated FWC estimates change by up to 50%, showing that we likely still do not have a robust estimate of FWC for the late winter and early spring time period.

Employing monthly and seasonal averaging periods, the net spring-to-fall ranges in FWC and HC anomalies are 140–190 km^3 and 2.3–2.6 $\times 10^{20}$ J, respectively. Lacking sufficient CTD data to make spatially explicit annual estimates of the Bering shelf seasonal FWC and HC variability, we turn to the long-term moored data set at NOAA site M2 (57°N, 167°W) for comparison (P. Stabeno, unpublished data). The 1995–2006 April–September mean freshening and heating measured at 10 and 60 m depths is typically −0.12 and 5.3 °C, respectively (with ranges of −0.03 to −0.2 and 2.3 to 8.3 °C). A −0.1 salinity change represents freshening by ~30 km^3 freshwater when integrated across the central shelf volume, and a warming of 5.3 °C represents a HC increase of 2.0 $\times 10^{20}$ J. Given the large temperature anomaly de-correlation scale, the M2 temperature record likely represents the seasonal HC increase on the shelf reasonably well. The salinity anomaly de-correlation scales are smaller, and so the M2 salinity record may not reflect the seasonal salinity decrease over the broader region.

We now compare the various flux terms to the observed seasonal FWC changes (Fig. 10). Following Aagaard et al. (2006), we use precipitation data collected at St. Paul Island and apply it uniformly to the entire region. We estimate evaporation from the NCEPR latent heat flux. For 1 April–1 September, $P-E$ for the central shelf is 23 km^3 on average.

Passive microwave satellite sea ice measurements provide surface area estimates of ice cover, but not of thickness. From 250 direct ice thickness measurements made between March and May in 2008 and 2009, the mean thickness was 0.4 m, and the mean ice salinity 6.4 (R. Gradinger, B. Bluhm and K. Iken, pers. comm.). Melting an ice pack with an area of 1.0 $\times 10^5$ km^2 (representing the northern half of our domain), thickness of 0.4 m, and ice density of 900 kg m^{-3} releases 36 km^3 of freshwater, which would reduce the salinity of the entire domain by 0.2 if distributed vertically over the entire water column, or by 0.85 if mixed over only the upper 10 m. Neglecting advection and applying the observed mean March/April ice extents (Table 1), the probable FW contribution from ice melt is 20–40 km^3.

A mean along-shelf flow of 2 cm s^{-1} (Schumacher and Kinder, 1983) traverses 250 km in 145 days. Ice melt and shelf water over the southeast shelf therefore likely remains within the integration domain through summer, while that on the northern shelf is advected away by the end of summer (Danielson et al., 2006). The mean spring–late winter salinity difference between the waters north and south of 60°N is 0.24 (Fig. 9), so along-isobath (northward) advection would tend to replace the higher salinity northern waters with fresher waters from the south, accounting for a freshening of ~20 km^3. This freshening tendency diminishes through summer as the northerly waters are flushed and eventually become fresher than the southerly waters due to offshore spreading of river discharge.

The Yukon (202 km^3 yr^{-1}) and Kuskokwim (38 km^3 yr^{-1}) rivers are the largest sources of freshwater to the inner-shelf. Coastal discharge increases rapidly from winter minima (Yukon, 900–1500 m^3 s^{-1}; Kuskokwim, 170–450 m^3 s^{-1}) to maxima in May or June (Yukon, 13 000–33 000 m^3 s^{-1}; Kuskokwim, 2000–11 000 m^3 s^{-1}). The cumulative 1 April–1 September discharge for both rivers averages 152 km^3. Most of this fresh water probably departs the shelf through Bering Strait (Coachman et al., 1975; Aagaard et al., 2006). Due to the paucity of data inshore of the 20 m isobath, the circulation and hydrography of the broad inner-shelf have not been described, however. Visible and infrared satellite imagery of sediment plumes and thermal structure suggest that frontal systems develop inshore of the 30 m isobath in summer. These fronts probably impede cross-shelf spreading of low-salinity coastal waters. This hypothesis is supported both by recent CTD data and drifter trajectories. For example, a July 2009 CTD transect along 62°N between the 55 and 7 m isobaths shows a strong temperature and salinity front inshore of the 20 m isobath (Fig. 11). Furthermore, in the summers of 2008 and 2009, drifters deployed in northern Kuskokwim Bay (Fig. 12) typically remained inshore of the 20 m isobath, slowly progressing northward past Nunivak Island. Below, we will also show that winds in summer are weak and not conducive to spreading freshwater offshore. In fall, however, drifters moved westward across the shelf. The 2008 and 2009 deployment results are consistent with the drifter trajectories shown by Danielson et al. (2006), which were deployed in September 2002, just north of Nunivak Island. Hence, while river discharge represents a substantial summer freshwater influx to the inner-shelf, most of it is probably retained nearshore and outside of our integration domain. Nevertheless, with on average 23 km^3 freshwater available from $P-E$, 29 km^3 from ice melt and 20 km^3 from along-shelf flow, less than one-half of the mean river discharge (152 km^3) needs to enter the integration domain to account for the observed April–September FWC increase of ~140 km^3 (Fig. 10).

The onset of the heating season (Fig. 13) occurs near the spring equinox, when the daily mean net surface heat flux switches from negative (oceanic heat loss) to positive (oceanic heat gain). We therefore compute the cumulative heat gain between 1 April (year

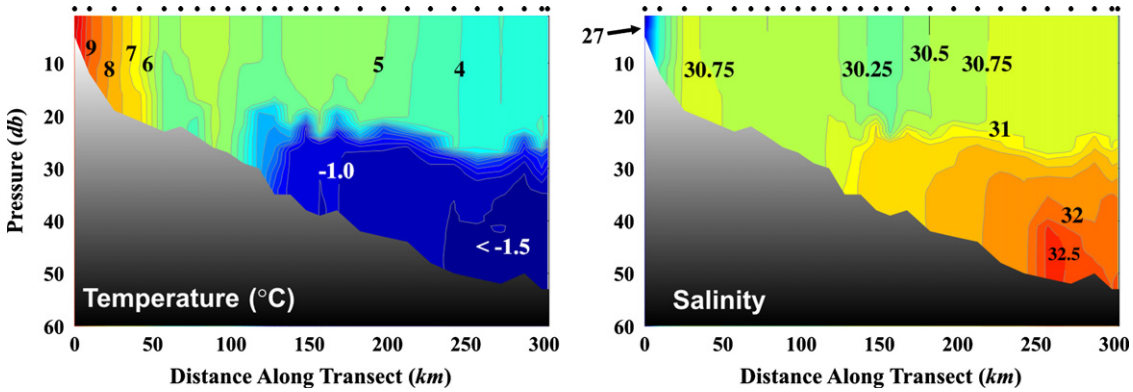

Fig. 11. CTD transect occupied on 15–16 July 2009 between 61.70°N, 166.31°W and 61.97°N, 171.98°W.

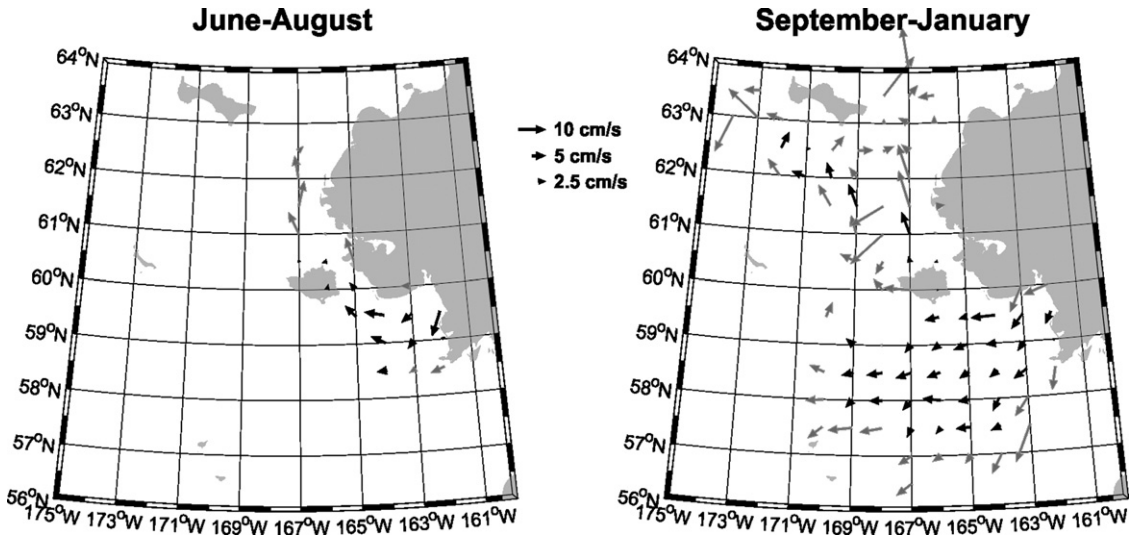

Fig. 12. Mean seasonal flow patterns derived from oceanographic drifters for June–August (left) and September–January (right). Black vectors denote grid cells with at least 30 drifter-days worth of data; gray vectors represent at least five drifter-days of data.

day 91) and 1 September (year day 244) using the NCEPR heat fluxes interpolated over our domain and, for comparison, repeat the calculation beginning on 1 May (year day 121). The seasonally integrated surface heat flux is 350 (300) EJ using the 1 April (1 May) start, so that regardless of the start date, the surface heat flux is sufficient to account for the observed heat gain of ~300 EJ (Fig. 10).

Similar to flushing the northern domain of saline water during summer, along-isobath advection would also flush the cold winter water, but could account for a mean seasonal HC increase of only ~35 EJ. We conclude that in the mean, seasonal advective heat fluxes are relatively small (~10% of the total flux) and of the same order as the heat budget uncertainty. This is consistent with the results of Reed and Stabeno (2002) who concluded that advective and diffusive processes amount to ~5% of the summer heat increase near mooring M2. More precise balancing of the seasonal mean heat budget will require substantially better knowledge of both the surface heat fluxes and of advection.

4.2. FWC interannual variability

For 2002–2007, the late summer range in FWC is ~130 km^3 (Table 2), which is similar to the mean FWC seasonal change noted in Section 4.1. There are no significant correlations among anomalies of end-of-summer FWC and sea ice melt, $P-E$, or discharge, neither individually nor when the fluxes are summed.

Because the end-of-summer FWC standard deviation (48.3 km^3) is not balanced by the variability of the runoff (18.4 km^3), $P-E$ (2.5 km^3), and ice melt (7.7 km^3) terms, other processes must also contribute. We compared a number of environmental time series at various time lags, including winds integrated over various time periods and regions, ice extent and retreat, river discharge, and salinities measured in the Gulf of Alaska at oceanographic station GAK1 (59.85°N, 149.47°W). Station GAK 1 is representative of the properties of the Gulf of Alaska coastal current that enters the Bering Sea shelf through Unimak Pass (Stabeno et al., 1995; Weingartner et al., 2005; Aagaard et al., 2006). Among these, only the cross-shelf Ekman transport (Table 2), derived from the preceding year's October–May along-shore wind stress, is significantly correlated ($r=-0.93$; $p=0.0072$) with FWC anomalies. Using NCEPR winds, the Ekman transports were estimated across the two line segments connecting the points (62.5°N, 167.5°W), (60°N, 167.5°W), and (58.5°N, 162°W), following the convention that offshore (onshore) transport is negative (positive). The cross-shelf Ekman transports would be particularly effective in changing the FWC, since they are directed along the shelf salinity gradient. Moreover the offshore flux begins in fall, when the salinity gradient is at its annual maximum. Presumably the fall winds also erode the frontal structure as river discharge diminishes, thus weakening the inner-front and enhancing the cross-shelf transport. This mechanism, which varies year-to-year, is also consistent with the drifter trajectories shown in Fig. 12.

An average cross-shore salinity difference of 1 is sufficient to supply the central shelf with ~60 km^3 of freshwater by offshore Ekman transport when integrated over the 2006 winter, although we do not know the actual cross-shelf salinity gradient through the winter months. In contrast, the on-shore component of Ekman transport in 2005 would have removed 70 km^3 of freshwater from the integration domain. Both of these fluxes are therefore of the proper magnitude and sign to nearly balance the FWC anomaly observed the following end-of-summer. Considering the shelf from a simplified two-dimensional perspective, upwelling of more saline subsurface waters would presumably replace the near surface low-salinity waters. In this case, the cross-shelf salt gradient would need to be only one-half of the value employed above in order to account for the observed FWC anomaly. It is not clear, however, what the role of upwelling onto the central shelf would be in a more realistic three-dimensional representation.

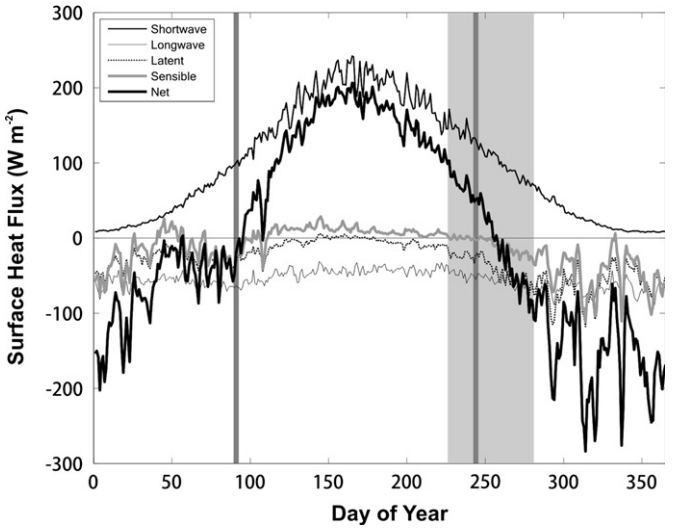

Fig. 13. Annual mean cycle of mean daily surface heat fluxes for the central shelf region over the years 2002–2007. Vertical gray lines denote 1 April and 1 September. The heating season begins on the date near 1 April when the net surface heat flux crosses from oceanic heat loss to oceanic heat gain. The BASIS cruises span days 226–281, depicted by the gray shading.

The Ekman transport computations, made across a two-segment transect, are sensitive to the changing orientation of the isobaths north and south of 60°N, so that merely using the winter mean north–south wind component does not yield a high correlation with the FWC anomaly. Inspection of Fig. 14 (second row) reveals that interannual differences in wind direction are just as pronounced as changes in magnitude. Indeed, there is a strong correlation ($r=-0.87$) between the FWC anomaly and the wind direction anomaly at 60°N, 170°W. The seasonal mean wind field in turn results from the large-scale atmospheric pressure distribution. Thus, years with the greatest positive FWC anomalies (and the largest westward Ekman transport over the shelf) coincide with low pressure over the northern Gulf of Alaska (Fig. 14). Note that other studies have also highlighted the importance of the zonal position of the Aleutian Low to a variety of problem sets, including those of Pease et al. (1982), Rodionov et al. (2005, 2007), Janout et al. (2010), Pickart et al. (2009), and Wang et al. (2009).

4.3. HC interannual variability

Integrating from 1 April to 1 September, we find a significant correlation between the net surface heat flux anomaly and the oceanic HC anomaly (Table 3). The summer surface heat flux anomaly standard deviation (11 EJ), however, represents only about 30% of the end-of-summer HC anomaly standard deviation (36.5 EJ). The end-of-winter HC standard deviation (16 EJ) accounts for ~40%, but it is not significantly correlated. Expressed in terms of percent variance accounted for, the summer heat flux anomaly and winter's end HC anomaly represent only 9% and 20% of the summer's end HC variance. The end-of-winter HC is estimated as follows. Convection and winter wind mixing produce a nearly

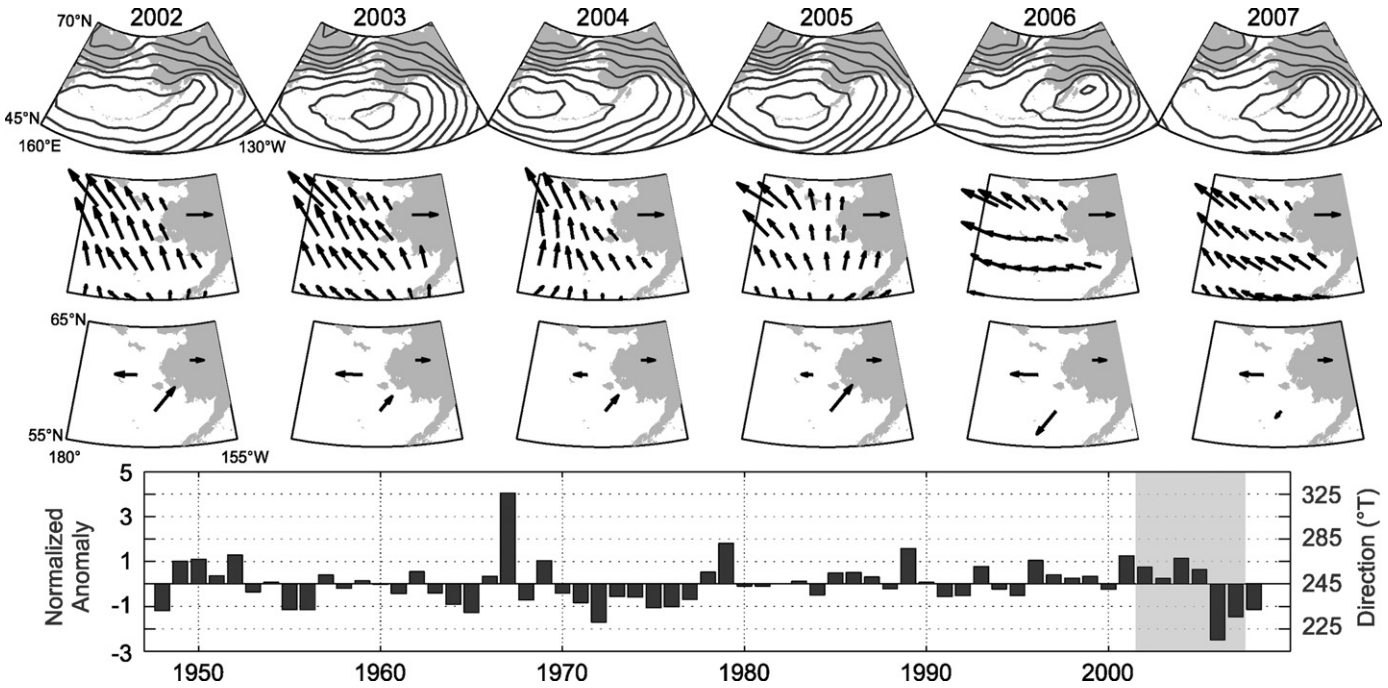

Fig. 14. Mean October–May 2002–2007 maps of sea level pressure (first row), maps of Ekman transport vectors (second row), maps of the cross-shore component of the Ekman transport for sub-domains north and south of 60°N (third row) and time series of the mean October–May 1948–2008 wind direction anomaly computed at 60°N, 170°W (bottom row). Sea level pressure is contoured at even integer millibar levels. High pressure exists in the lower right corner of all panels; closed contours bound low pressure minima. Scale vectors on land denote 5.3×10^2 kg s^{-1} m^{-1} and 5.0×10^4 m^3 s^{-1} for the second and the third rows, respectively.

homogeneous end-of-winter water column (Stabeno et al., 2001; Stabeno et al., 2002). Over the mean March and April shelf area occupied by sea ice with concentrations $>30\%$, we assume a near-freezing mean water column temperature of $-1.5\,^{\circ}C$ and over the region with sea ice concentrations $<30\%$ we assume a mean water column temperature of $+2\,^{\circ}C$. The former value is likely good to within $-0.3/+1.5\,^{\circ}C$, the latter to $\pm 2\,^{\circ}C$, based on ERSST data, NOAA mooring M2 records (P. Stabeno, unpublished data), and CTD profiles (Reed, 1995). The end-of-winter HC computed using these extremes does not vary by more than 25%.

Can advective heat fluxes account for the unexplained portion of the heat balance? We address this by using the heat balance equation

$$\underbrace{H_{se}}_{\substack{\text{end-of-summer}\\ \text{heat content}}} = \underbrace{H_{we}}_{\substack{\text{end-of-winter}\\ \text{heat content}}} - \underbrace{H_l}_{\substack{\text{heat required}\\ \text{to melt ice}}} + \underbrace{\int\int\int Q_s\,dt\,dx\,dy}_{\substack{\text{Apr. 1 to Sept. 1}\\ \text{surface heat flux}}} + \underbrace{\int v\frac{\partial H}{\partial y}\,dt}_{\substack{\text{alongshelf}\\ \text{heat flux}}}. \quad (3)$$

We can estimate all terms except the along-shelf velocity (v). For example, we estimate H_{we} as described above. Cross-shelf transport is neglected, which is consistent with the summer drifter data (Fig. 12). We then find that the along-shelf velocity fluctuations required to balance the heat budget anomalies are $\pm 2\ cm\ s^{-1}$.

We can also estimate the surface Ekman transport. For 1 April–1 September, the along-isobath Ekman transport anomalies computed across latitude 60°N are significantly correlated with the end-of-summer HC anomalies (Table 3), although the cross-isobath Ekman transport is not. While compensating return flows in the bottom Ekman layer could support differential heat advection in subsurface waters, the along-isobath thermal gradients below the MLD are much smaller than those above the MLD (Fig. 4) and are thus ignored. Assuming an Ekman depth equal to a typical mid-shelf summer mixed layer depth ($\sim$20 m), the mean along-shelf Ekman velocity is 0.1 cm s^{-1}, and the 2002–2007 range is between -1 and $+1$ cm s^{-1}, about half that estimated from the heat budget and of the right magnitude to satisfy Eq. (3).

The atmospheric conditions responsible for the correlation between the along-shelf velocity and HC anomaly are evident in the sea level pressure maps and associated Ekman transport vectors presented in Fig. 15. In 2004, the warmest year encountered during the BASIS surveys, a deep Aleutian Low developed over the western Bering Sea while high pressure characterized the Alaskan mainland, resulting in strong northward Ekman transport over the shelf. The coldest 2 years, 2006 and 2007, had mean westward/southwestward transport over the shelf, resulting from a split Aleutian Low pattern manifested by closed sea level pressure contours in both the northern Gulf of Alaska and the western Bering Sea.

In summary, both the heat budget and Ekman transport estimates of the along-isobath summer heat flux show similar magnitudes and year-to-year trends (not shown), strongly suggesting that variability in the along-shelf flow accounts for much of the interannual variability observed in the end-of-summer integrated HC.

5. Discussion and concluding remarks

Central shelf waters respond with nearly equal magnitude to the mean seasonal cycle of thermohaline forcing and to interannual differences in the regional wind forcing. Our estimates of the HC and FWC budgets indicate that while we can reasonably account for the April–September increases in HC and FWC, improved data sets with an emphasis on advective estimates are required to tighten these budgets. Nevertheless, the observations in hand are sufficient

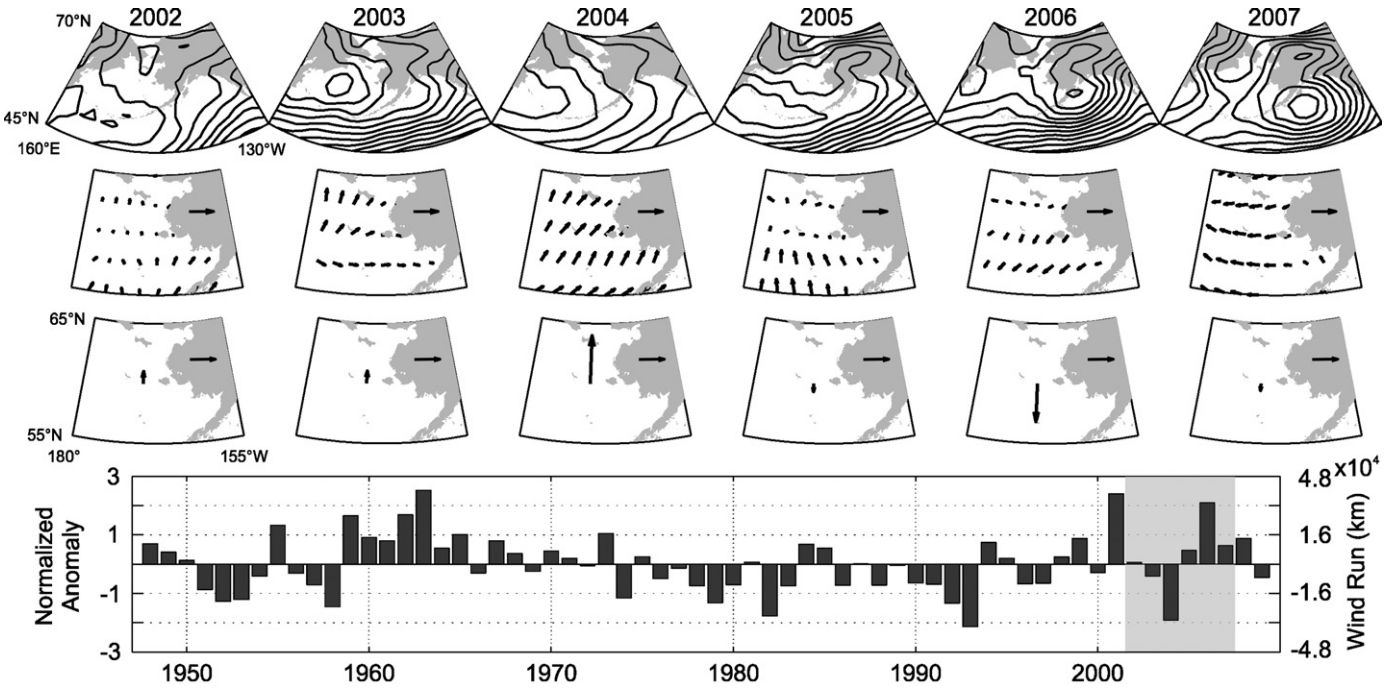

Fig. 15. Mean April–August 2002–2007 maps of sea level pressure (first row), maps of Ekman transport vectors (second row), maps of the Ekman transport N–S component across 60°N (third row) and time series of the mean April–August 1948–2009 E–W wind run anomaly computed at 60°N, 170°W (bottom row). Sea level pressure is contoured at all integer millibar levels. High pressure exists in the lower right corner of all panels; closed contours bound low pressure minima. Scale vectors on land denote 5.3×10^{2} kg m^{-1} s^{-1} and 2.0×10^{4} m^{3} s^{-1} for the second and the third rows, respectively.

to show that interannual HC and FWC anomalies generally do not co-vary because HC anomalies result in large part from variability in along-isobath advection during spring and summer months, whereas FWC anomalies depend substantially on cross-isobath advection during fall and winter. In both cases, the Ekman transport is determined by the seasonal mean zonal position of the Aleutian Low.

Results from the correlation maps, Ekman transport computations, and drifter releases are all consistent with the hypothesis that winter cross-isobath exchange is an important control of salinity variability on this shelf. Inspection of estimated monthly mean surface Ekman transports (Fig. 16) shows that particularly in October and November, shelf surface flows are driven westward across the isobaths. The wind-driven cross-shelf flux occurs to a greater or lesser degree each winter (Fig. 14 and Table 2), resulting in a near-shore/mid-shelf inverse correlation (Fig. 8) of salinities. In years that the Aleutian Low is displaced eastward, Ekman transport helps flush the nearshore region to the middle shelf. In years that the Aleutian Low is displaced westward, the fresh coastal waters tend to be trapped to the coast and/or are advected northward.

Cross-isobath exchange has implications for macronutrient (Whitledge and Luchin, 1999) and micronutrient (Aguilar-Islas et al., 2007) transport and biological utilization, as well as for the transport of passively drifting eggs and larvae (Wespestad et al., 2000; Lanksbury et al., 2007). In addition to carrying coastal waters to the mid-shelf region, iron-rich shelf water (Aguilar-Islas et al., 2007) may be carried still farther seaward to the productive continental slope (Springer et al., 1996) and deep basin, while compensating flows transport mid- and outer-shelf waters landward, helping resupply nitrate to these shallower waters. Whether westward advection to the basin acts as a significant sink for Yukon and Kuskokwim discharge is at this point unclear, but highly relevant to determining the formation and modification of water masses on the Bering shelf and their subsequent northward advection (Coachman et al., 1975). The issue is particularly important because the Bering Strait throughflow accounts for a large percentage of the Arctic Ocean freshwater input (Aagaard and Carmack, 1989; Dickson et al., 2007) and so ultimately impacts both Arctic Ocean stratification and conditions in the North Atlantic (Aagaard et al.,1981; Goosse et al., 1997; Peterson et al., 2002; Woodgate and Aagaard, 2005).

The time series of Figs. 14 and 15 place the 2002–2007 mean October–May and April–August wind anomalies within a 60-year historical context. The October–May normalized wind direction anomaly at 60°N, 170°W (correlation to FWC anomaly: $r=-0.87$, $p=0.023$) is a surrogate for the winter cross-isobath Ekman transport. The mean October–May wind direction is toward 225°N. This parameter is normally distributed with a standard deviation of 20°, and so a two-standard deviation anomaly is equivalent to a rotation of 40° away from the mean winter wind direction; the NCEPR directional range is 133°. The 2002–2007 time period includes no outstanding positive anomalies, but 2006 and 2007 stand out as the lowest (-2.5) and third lowest (-1.5) anomalies since 1948. Strikingly, 2006–2008 is the first 3-year period since the mid-1970 s regime shift (Hare and Mantua, 2000) to exhibit three negative anomalies in a row. The April–August net zonal wind run (mean wind speed multiplied by time) anomaly at 60°N, 170°W (correlation to HC anomaly: $r=-0.87$, $p=0.024$) is a measure of the along-isobath summer Ekman transport; negative values reflect easterly winds that promote northward Ekman transport. Fig. 15 shows that 2004 and 2006 are notably anomalous, ranking as the second lowest (-1.9) and third highest ($+2.1$) anomaly years over the record, respectively. Taken together, Figs. 14 and 15 show that the Bering shelf system has many possible states. Indeed, the two 60-year time series are uncoupled from each other ($r=0.21$, $p=0.10$).

In this effort we have identified mechanisms that likely modulate or control the thermal and haline properties of the central Bering Sea

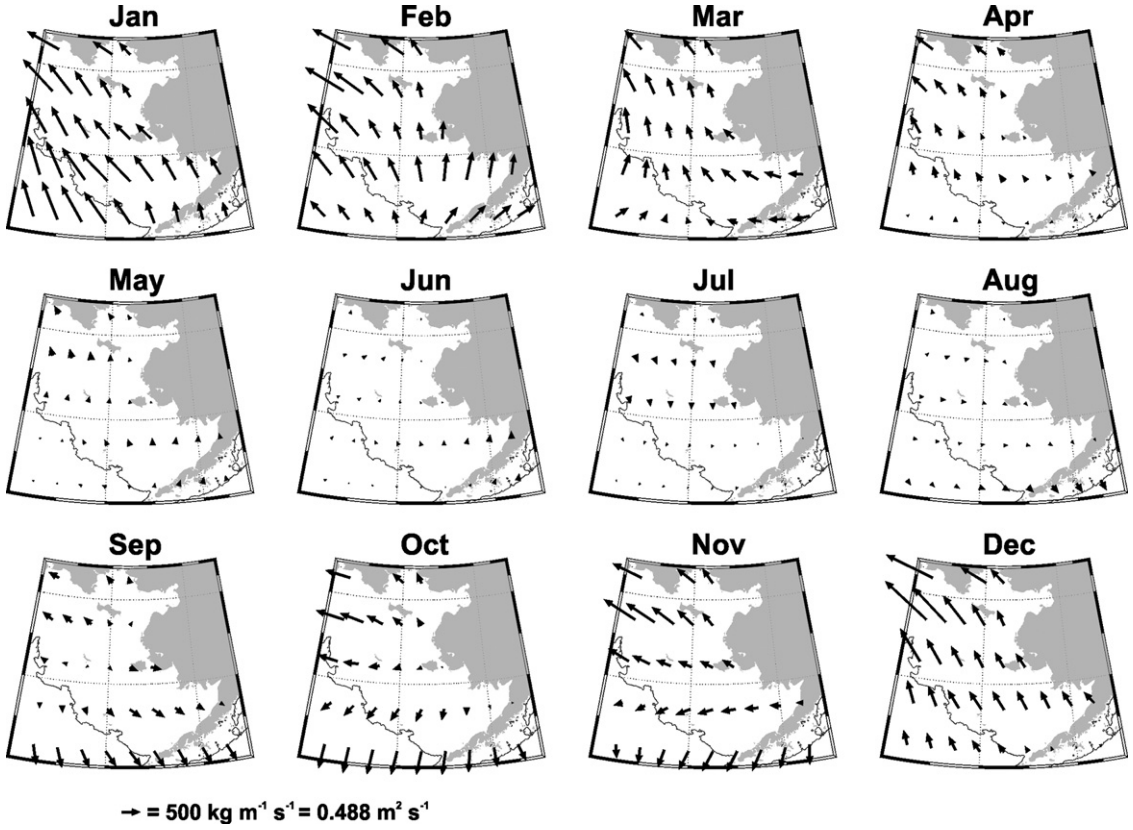

Fig. 16. Mean monthly Ekman transport computed from the NCEPR 6-hourly wind fields between 2002 and 2007.

shelf. For example, wind-driven transport changes appear to determine the interannual variability of both FWC and HC. While these ideas are promising, our analysis is based on a limited data set. Future studies will need to assess whether or not our hypotheses and conclusions are robust, as well as to rigorously quantify the various fluxes that we can only crudely estimate (e.g., Whitney and Garvine, 2005; Fewings et al., 2008). Although we have suggested chemical and biological components that may be sensitive to the proposed processes and circulation schemes, a proper assessment of the impacts on nutrients, primary productivity, and larval transport, for example, will likely prove to be significantly challenging undertakings, as will certainly be the extent to which these physical processes influence the broader ecosystem.

Acknowledgments

This manuscript would not have been possible without the cross-institutional and cross-disciplinary collaboration that has been fostered through the BASIS and BEST programs. We particularly thank Ed Farley and the rest of the BASIS scientists at NOAA/AFSC for their support. Many thanks to Kristin Cieciel for survey logistics, oceanographic data collection, CTD data processing, and database maintenance; John Pohl and Alex Andrews for oceanographic data collection; Jennifer Lanksbury for database design and maintenance; Rolf Gradinger, Katrin Iken, and Bodil Bluhm for sharing their ice station data; and Phyllis Stabeno for sharing M2 mooring data and BEST CTD data, both collected with the support of the NOAA/PMEL Eco-FOCI program. We thank the dedicated crews of the F/V *Sea Storm*, F/V *NW Explorer*, R/V *Oscar Dyson*, R/V *Knorr*, R/V *Point Sur*, and the *USCGC Healy* for the many successful BASIS and BEST cruises. We thank the BEST program scientists and field crews for the CTD data collections and processing. Data from NSF sponsored BEST cruises HLY-07-01, HLY-08-03, and KN195-10 were taken under the direction of chief scientist R. Sambrotto, Lamont-Doherty Earth Observatory, Palisades, NY; data from cruise HLY-08-02 were taken under the direction of chief scientist Carin Ashjian, Woods Hole Oceanographic Institute, Woods Hole, MA; and data from cruise HLY-09-01 were taken under the direction of chief scientist Lee Cooper, University of Maryland Center for Environmental Science, Solomons, MD. The manuscript was improved with valuable comments from two anonymous reviewers. BASIS oceanographic data collection was funded by the Arctic-Yukon-Kuskokwim Sustainable Salmon Initiative, the Bering Sea Fisherman's Association, NOAA Fisheries and the Environment (FATE) program, and the National Marine Fisheries Service. Drifter data were collected under funding from the North Pacific Research Board, Grant NPMRI T2130, and the Arctic Yukon Kuskokwim Sustainable Salmon Initiative, Grant ADN #1195952. This manuscript is listed as BEST/BSIERP Publication #6. K. Aagaard was supported by NSF Grant ARC-0732428. S. Danielson and T. Weingartner received financial support from the Bering Sea Fisherman's Association Grant AC-299 and NSF Grant ARC-0732771.

References

Aagaard, K., Coachman, L.K., Carmack, E.C., 1981. On the halocline of the Arctic Ocean. Deep Sea Research 28, 529–545.

Aagaard, K., Carmack, E., 1989. The role of sea-ice and other freshwater in the Arctic circulation. Journal of Geophysical Research 94, 14485–14498. doi:10.1029/89JC01375.

Aagaard, K., Weingartner, T.J., Danielson, S.L., Woodgate, R.A., Johnson, G.C., Whitledge, T.E., 2006. Some controls on flow and salinity in Bering Strait. Geophysical Research Letters 33, L19602. doi:10.1029/2006GL026612.

Aguilar-Islas, A.M., Hurst, M., Buck, K., Sohst, B., Smith, G.J., Lohan, M.C., Bruland, K.W., 2007. Micro- and macronutrients in the southeastern Bering Sea: insight into iron-replete and iron-depleted regimes. Progress in Oceanography 73 (2), 99–126. doi:10.1016/j.pocean.2006.12.002.

Alexander, V., Niebauer, H.J., 1981. Oceanography of the Eastern Bering Sea Ice-Edge Zone in spring. Limnology and Oceanography Vol. 26 (6), 1111–1125.

Aydin, K., Mueter, F., 2007. The Bering Sea—a dynamic food web perspective. Deep Sea Research Part II: Topical Studies in Oceanography 54 (23–26), Effects of Climate Variability on Sub-Arctic Marine Ecosystems—A GLOBEC Symposium, GLOBEC-ESSAS Symposium on Effects of Climate Variability on Sub-Arctic Marine Ecosystems, pp. 2501–2525, ISSN 0967-0645, doi:10.1016/j.dsr2.2007.08.022.

Bond, N.A., Overland, J.E., Turet, P., 1994. Spatial and temporal characteristics of the wind forcing of the Bering Sea. Journal of Climate 7 (7), 1119–1130.

Bond, N.A., Overland, J.E., 2005. The importance of episodic weather events to the ecosystem of the Bering Sea shelf. Fisheries Oceanography 14 (2), 97–111.

Bowers, F.R., Schwenzfeier, M., Milani, K., Salmon, M., Herring, K., Shaishnikoff, J., El Russ, R., Burt, Barnhart, H., 2008. Annual Management Report for the Commercial and Subsistence Shellfish Fisheries of the Aleutian Islands, Bering Sea and the Westward Region's Shellfish Observer Program, 2007/08, Fishery Management Report 08-73. Alaska Department of Fish and Game 255 pp.

Boyer, T.P., Antonov, J.I., Garcia, H.E., Johnson, D.R., Locarnini, R.A., Mishonov, A.V., Pitcher, M.T., Baranova, O.K., Smolyar, I.V., 2006. World Ocean Database 2005. In: Levitus, S. (Ed.), NOAA Atlas NESDIS 60. U.S. Government Printing Office, Washington, DC, pp. 190.

Boyer, T.P., Antonov, J.I., Baranova, O.K., Garcia, H.E., Johnson, D.R., Locarnini, R.A., Mishonov, A.V., O'Brien, T.D., Seidov, D., Smolyar, I.V., Zweng, M.M., 2009. World Ocean Database, 2009. In: Levitus, S. (Ed.), NOAA Atlas NESDIS 66. U.S. Gov. Printing Office, Washington, DC, pp. 216.

Brower Jr., W.A., Baldwin, R.G., Williams Jr., C.N., Wise, J.L., Leslie, L.D., 1988. Climate Atlas of the Outer Continental Shelf Waters and Coastal Regions of Alaska, vol. 3, Chukchi-Beaufort Sea. Natl. Clim. Data Cent., Asheville, NC 497 pp.

Chapman, D.C., Lentz, S.J., 1994. Trapping of a coastal density front by the bottom boundary layer. Journal of Physical Oceanography 24, 1464–1479.

Chapman, D.C., Lentz, S.J., 1997. Adjustment of stratified flow over a sloping bottom. Journal of Physical Oceanography 27, 340–356.

Coachman, L.K., Aagaard, K., Tripp, R.B., 1975. Bering Strait: The Regional Physical Oceanography. University of Washington Press, Seattle 172 pp.

Coachman, L.K., 1986. Circulation, water masses and fluxes on the southeastern Bering Sea shelf. Continental Shelf Research 5, 23–108.

Comiso, J., 1999. Bootstrap Sea Ice Concentrations from NIMBUS-7 SMMR and DMSP SSM/I, (1979–2007). National Snow and Ice Data Center. Digital media, Boulder, CO, USA updated 2008.

Danielson, S., Aagaard, K., Weingartner, T., Martin, S., Winsor, P., Gawarkiewicz, G., Quadfasel, D., 2006. The St. Lawrence polynya and the Bering shelf circulation: new observations that test the models. Journal of Geophysical Research J111, C09023. doi:10.1029/2005JC003268.

Davis, R.E., 1985. Drifter observations of coastal surface currents during CODE: the method and descriptive view. Journal of Geophysical Research 90, 4741–4755.

Dickson, R., Rudels, B., Dye, S., Karcher, M., Meincke, J., Yashayaev, I., 2007. Current estimates of freshwater flux through Arctic and subarctic seas. Progress in Oceanography 73 (3–4),Observing and Modelling Ocean Heat and Freshwater Budgets and Transports, May–June 2007. doi:10.1016/j.pocean.2006.12.003, pp. 210–230.

Drucker, R., Martin, S., Moritz, R., 2003. Observations of ice thickness and frazil ice in the St. Lawrence Island polynya from satellite imagery, upward looking sonar, and salinity/temperature moorings. Journal of Geophysical Research 108 (C5), 3149. doi:10.1029/2001JC001213.

Failor-Rounds, B., 2005. Bering Sea–Aleutian Islands Area State-Waters Groundfish fisheries and Groundfish harvest from parallel seasons in 2004. Alaska Department of Fish and Game, Fishery Management Report No. 05-71, Anchorage.

Fewings, M., Lentz, S.J., Fredericks, J., 2008. Observations of cross-shelf flow driven by cross-shelf winds on the inner continental shelf. Journal of Physical Oceanography 38, 2358–2378.

Gawarkiewicz, G., Chapman, D.C., 1992. The role of stratification in the formation and maintenance of shelfbreak fronts. Journal of Physical Oceanography 22, 753–772.

Goosse, H., Campin, J.-M., Fichelet, T., Deleersnijder, E., 1997. Sensitivity of a global ice-ocean model to the Bering Strait throughflow. Climate Dynamics 13, 349–358.

Grebmeier, J.M., Overland, J.E., Moore, S.E., Farley, E.V., Carmack, E.C., Cooper, L.W., Frey, K.E., Helle, J.H., McLaughlin, F.A., McNutt, S.L., 2006. A major ecosystem shift in the northern Bering Sea. Science 311 1461–146.

Hare, S.R., Mantua, N.J., 2000. Empirical evidence for northeast Pacific regime shifts in 1977 and 1989. Progress in Oceanography 47, 103–145.

Janout, M.A., Weingartner, T.J., Royer, T.C., Danielson, S.L., 2010. On the nature of winter cooling and the recent temperature shift on the northern Gulf of Alaska shelf. J. Geophys. Res. 115, C05023, doi:10.1029/2009JC005774.

Kinder, T.H., Schumacher, J.D., 1981a. Hydrographic structure over the continental shelf of the southeastern Bering Sea. In: Hood, D.W., Calder, J.A. (Eds.), The Eastern Bering Sea Shelf, Oceanography and Resources, Vol. 1. University of Washington, pp. 31–52.

Kinder, T.H., Schumacher, J.D., 1981b. Hydrographic structure over the continental shelf of the southeastern Bering Sea. In: Hood, D.W., Calder, J.A. (Eds.), The Eastern Bering Sea Shelf, Oceanography and Resources, vol. 1. University of Washington, pp. 53–75.

Kalnay, E., Kanamitsu, M., Kistler, R., Collins, W., Deaven, D., Gandin, L., Iredell, M., Saha, S., White, G., Woollen, J., Zhu, Y., Chelliah, M., Ebsuzaki, W., Higgins, W., Janowiak, J., Mo, K.C., Ropelewski, C., Wang, J., Leetma, A., Reynolds, R., Jenne, R., Joseph, D., 1996. The NCEP/NCAR 40-year reanalysis project. Bulletin of the American Meteorological Society 77, 437–470.

Ladd, C., Bond, N., 2002. Evaluation of the NCEP/NCAR reanalysis in the NE Pacific and the Bering Sea. Journal of Geophysical Research 107 (C10). doi:10.1029/2001JC001157.

Lanksbury, J.A., Duffy-Anderson, J.T., Mier, K.L., Busby, M.S., Stabeno, P.J., 2007. Distribution and transport patterns of northern rock sole, *Lepidopsetta polyxystra*, larvae in the southeastern Bering Sea. Progress In Oceanography 72 (1), 39–62. doi:10.1016/j.pocean.2006.09.001.

Lowry, L.F., Frost, K.J., Calkins, D.G., Swartzman, G.L., Hills, S., 1982. Feeding habits, food requirements and status of Bering Sea marine mammals. Counc. Doc. Nos. 19 and 19 A (annotated bibliography), North Pacific Fisheries Management Council, P.O. Box 103136, Anchorage, AK 99510, 574 pp.

Mendenhall, W., Sincich, T., 1988. Statistics for the Engineering and Computer Sciences, 2nd ed. Dellen Publishing Co., San Fransisco, CA ISBN 0-02-380460-2, 1036 pp.

Mizobata, K., Saitoh, S., 2004. Variability of Bering Sea eddies and primary productivity along the shelf edge during 1998–2000 using satellite multisensor remote sensing. Journal of Marine Systems 50, 101–111.

McNutt, L., 1981. Remote sensing analysis of ice growth and distribution in the eastern Bering Sea, March 1979. In: Hood, D.W., Calder, J.A. (Eds.), The Eastern Bering Sea Shelf, Oceanography and Resources, vol. 1. University of Washington, pp. 141–166.

Muench, R., Ahlnas, K., 1976. Ice movement and distribution in the Bering Sea from March to June 1974. Journal of Geophysical Research 81 (24), 4467–4476.

Niebauer, H.J., Schell, D.M., 1993. Physical environment of the Bering Sea population. In: Burns, J.J., Montague, J.J., Cowles, C.J. (Eds.), The Bowhead Whale. Allen Press, Lawrence, Kans, pp. 23–44.

Niebauer, H.J., Bond, N.A., Yakunin, L.P., Plotnikov, V.V., 1999. An update on the climatology and sea ice of the Bering Sea. In: Loughlin, T.R., Ohtani, K. (Eds.), Dynamics of the Bering Sea. University of Alaska Sea Grant College Program (AK-SG-99-03), Fairbanks, AK, pp. 29–59.

Overland, J.E., Pease, C.H., 1982. Cyclone climatology of the Bering Sea and its relation to sea ice extent. Monthly Weather Review 110, 5–13.

Overland, J.E., Salo, S.A., Kantha, L.H., Clayson, C.A., 1999. Thermal stratification and mixing on the Bering Sea shelf. In: Loughlin, T.R., Ohtani, K. (Eds.), Dynamics of the Bering Sea: A Summary of Physical, Chemical, and Biological Characteristics, and a Synopsis of Research on the Bering Sea, University of Alaska Sea Grant, AK-SG-99-03. North Pacific Marine Science Organization (PICES), pp. 129–146.

Overland, J.E., Bond, N.A., Adams, J.M., 2002. The relation of surface forcing of the Bering Sea to large-scale climate patterns. Deep-Sea Research, Part II 49 (26), 5855–5868.

Pease, C.H., 1981. Eastern Bering Sea ice dynamics and thermodynamics (Chapter 13). In: Hood, D.W., Calder, J.A. (Eds.), Eastern Bering Sea Shelf: Oceanography and Resources, vol. 1. USDOC/NOAA/OMPA, pp. 213–222.

Pease, C.H., Schoenberg, S.A., Overland, J.E., 1982. A climatology of the Bering Sea and its relation to sea ice extent. NOAA Technical Report ERL 419-PMEL 36, NTIS: PB82-246950, 29 pp.

Peterson, B.J., Holmes, R.M., McClelland, J.W., Vörösmarty, C.J., Lammers, R.B., Shiklomanov, A.I., Shiklomanov, I.A., Rahmstrof, S., 2002. Increasing river discharge to the Arctic Ocean. Science 298, 2171–2173. doi:10.1126/science.1077445.

Pickart, R.S., Moore, G.W.K., Macdonald, A.M., Renfrew, I.A., Walsh, J.E., Kessler, W.S., 2009. Seasonal evolution of Aleutian low-pressure systems: implications for North Pacific sub-polar circulation. Journal of Physical Oceanography 39, 1317–1339.

Reed, R.K., 1978. The heat budget of a region in the eastern Bering Sea, summer 1976. Journal of Geophysical Research 83, 3635–3645.

Reed, R.K., 1995. Water poperties over the Bering Sea shelf: climatology and variations. NOAA Technical Report ERL 452-PMEL 42, 15 pp.

Reed, R.K., Stabeno, P.J., 2002. Surface heat fluxes and subsurface heat content at a site over the southeastern Bering Sea shelf, May–June 1996. Deep-Sea Research, Part II 49, 5911–5917.

Rodionov, S.N., Overland, J.E., Bond, N.A., 2005. The Aleutian Low and winter climatic conditions of the Bering Sea. Part I: Classification. Journal of Climate 18 (1), 160–177.

Rodionov, S.N., Bond, N.A., Overland, J.E., 2007. The Aleutian Low, storm tracks, and winter climate variability in the Bering Sea. Deep-Sea Research, Part II 54 (23–26), 2560–2577.

Rouault, M., Reason, C.J.C., Lutjeharms, J.R.E., Beljaars, A.C.M., 2003. Underestimation of latent and sensible heat fluxes above the Agulhas Current in NCEP and ECMWF analyses. Journal of Climate 16, 776–782.

Sea-Bird Instruments, Inc (SBE), 2009. SEASOFT V2: SBE Data Processing Users Manual. Sea-Bird Electronics, Inc., Bellevue, Washington 145 pp.

Sambrotto, R.N., Niebauer, H.J., Georing, J.J., Iverson, R.L., 1986. Relationships among vertical mixing, nitrate uptake and phytoplankton growth during the spring bloom in the southeast Bering Sea middle shelf. Continental Shelf Research 5, 161–198.

Sambrotto, R.N., Mordy, C., Zeeman, S.I., Stabeno, P.J., Macklin, S.A., 2008. Physical forcing and nutrient conditions associated with patterns of Chl a and phytoplankton productivity in the southeastern Bering Sea during summer. Deep-Sea Research, Part II 55 (16–17), 1745–1760.

Schumacher, J., Aagaard, K., Pease, C., Tripp, R., 1983. Effects of a shelf polynya on flow and water properties in the northern Bering Sea. Journal Geophysical Research 88 (C5), 2723–2732.

Schumacher, J.D., Kinder, T.H., 1983. Low-frequency current regimes over the Bering Sea shelf. Journal of Physical Oceanography 13, 607–623.

Schumacher, J.D., Reed, R.K., 1992. Characteristics of currents over the continental slope of the eastern Bering Sea. Journal of Geophysical Research 97 (C6), 9423–9433.

Scott, J.D., Alexander, M.A., 1999. Net shortwave fluxes over the ocean. Journal of Physical Oceanography 29, 3167–3174.

Smith, S.R., Legler, D.M., Verzone, K.V., 2001. Quantifying uncertainties in NCEP reanalyses using high-quality research vessel observations. Journal of Climate 14, 4062–4072.

Smith, T.M., Reynolds, R.W., Peterson, Thomas C., Lawrimore, Jay, 2008. Improvements to NOAA's historical merged land–ocean surface temperature analysis (1880–2006). Journal of Climate 21, 2283–2296.

Springer, A., McRoy, C.P., Flint, M., 1996. The Bering Sea Green Belt: shelf-edge processes and ecosystem production. Fisheries Oceanography 5, 205–223.

Stabeno, P.J., Reed, R.K., Schumacher, J.D., 1995. The Alaska Coastal Current: continuity of transport and forcing. Journal of Geophysical Research 100, 2477–2485.

Stabeno, P.J., Van Meurs, P., 1999. Evidence of episodic on-shelf flow in the southeastern Bering Sea. Journal of Geophysical Research 104 (C12), 720 29, 715–729.

Stabeno, P.J., Bond, N.A., Kachel, N.B., Salo, S.A., Schumacher, J.D., 2001. On the temporal variability of the physical environment over the south-eastern Bering Sea. Fisheries Oceanography 10 (1), 81–98.

Stabeno, P.J., Kachel, N.B., Sullivan, M., Whitledge, T.E., 2002. Variability of physical and chemical characteristics along the 70-m isobath of the southeast Bering Sea. Deep-Sea Research, Part II 49 (26), 5931–5943.

Takenouti, A.Y., Ohtani, K., 1974. Currents and water masses in the Bering Sea: a review of Japanese work. In: Hood, D.W., Kelley, E.J. (Eds.), Oceanography of the Bering Sea. Occasional Publication No. 2, Institute of Marine Science, University of Alaska Fairbanks, pp. 39–57.

Taylor, P.K., 2000. Intercomparison and validation of ocean–atmosphere energy flux fields. In: Taylor, P.K. (Ed.), Final Report of the Joint World Climate Research program and Scientific Committee on Ocean Research Working Group on Air–Sea Fluxes. World Climate Research Program Report WCRP-112, 303 pp.

UNESCO, 1994. Protocols for the Joint Global Ocean Flux Study (JGOFS) Core Measurements. IOC Manual and Guides, 29.

Wang, J., Hu, H., Mizobata, K., Saitoh, S., 2009. Seasonal variations of sea ice and ocean circulation in the Bering Sea: a model-data fusion study. Journal of Geophysical Research 114 (C02011). doi:10.1029/2008JC004727.

Walsh, J.J., McRoy, C.P., Coachman, L.K., Goering, J.J., Nihoul, J.J., Whitledge, T.E., Blackburn, T.H., Parker, P.L., Wirick, C.D., Shuert, P.G., Grebmeier, J.M., Springer, A.M., Tripp, R.D., Hansell, D.A., Djenidi, S., Deleersnijder, E., Henriksen, K., Lund, B.A., Andersen, P., Muller-Karger, F.E., Dean, K., 1989. Carbon and nitrogen cycling within the Bering Chukchi seas: source regions for organic matter effecting AOU demands of the Arctic Ocean. Progress in Oceanography 22 (4), 277–358.

Weingartner, T.J., Danielson, S., Royer, T.C., 2005. Freshwater variability and predictability in the Alaska Coastal Current. Deep-Sea Research 52, 169–192.

Weller, R.A., Baumgartner, M.F., Josey, S.A., Fisher, A.S., Kindle, J.C., 1998. Atmospheric forcing in the Arabian Sea during 1994–1995: observations and comparison with climatological models. Deep-Sea Research 45, 1961–1999.

Wespestad, V.G., Fritz, L.W., Ingraham, W.J., Megrey, B.A., 2000. On relationships between cannibalism, climate variability, physical transport, and recruitment success of Bering Sea walleye pollock (*Theragra chalcogramma*). ICES Journal of Marine Science 57, 268–274.

Whitledge, T.E., Luchin, V.A., 1999. Summary of chemical distributions and dynamics in the Bering Sea. In: Loughlin, T.R., Ohtani, K. (Eds.), Dynamics of the Bering Sea. University of Alaska Sea Grant, Fairbanks, AK, pp. 217–249.

Whitney, M.M., Garvine, R.W., 2005. Wind influence on a coastal buoyant outflow. Journal of Geophysical Research 110, C03014. doi:10.1029/2003JC002261.

Woodgate, R.A., Aagaard, K., 2005. Revising the Bering Strait freshwater flux into the Arctic Ocean. Geophysical Research Letters 32, L02602. doi:10.1029/2004GL021747.

Zheng, J., Kruse, G.H., 2006. Recruitment variation of eastern Bering Sea crabs: climate forcing or top-down effects? Progress in Oceanography 68, 184–204.